# Quantum Monte Carlo Study of Frustrated Systems

# 阻錯系統的量子門特卡洛研究

HU, Feiming

胡飛鳴

A Thesis Submitted in Partial Fulfillment
of the Requirements for the Degree of
Doctor of Philosophy
in
Physics

The Chinese University of Hong Kong
August 2010

Thesis/Assessment Committee

Professor YU, Kin Wah (Chair)
Professor LIN, Hai Qing (Thesis Supervisor)
Professor LIU, Renbao (Committee Member)
Professor FENG, Shiping (External Examiner)

Abstract of thesis entitled:

Quantum Monte Carlo Study of Frustrated Systems

Submitted by HU, Feiming

for the degree of PhD of Philosophy

at The Chinese University of Hong Kong in July 2010

In this research thesis, we mainly study three strongly correlated systems: Hubbard model in bilayer triangular lattice which corresponds to the real material of $Na_xCoO_2 \cdot yH_2O$, strong-interaction electrons in graphene system and Anderson impurity in graphene. Our numerical method is determinant quantum Monte Carlo method which will be introduced in the chapter 2.

In the chapter 3, we study ferromagnetic fluctuations on two types of bilayer triangular lattices by the single-band Hubbard

model. We start from the tight-binding model to obtain energy spectrum, the density of sates, and the spin susceptibility. With finite Coulomb interaction turned on, we apply the random phase approximation and use the determinant quantum Monte Carlo method to study spin susceptibility for the two bilayer triangular lattices and make comparisons of their magnetic properties. The effects of the interlayer coupling is also examined in detail.

In the chapter 4, we addresses the issue of the ferromagnetism in graphene-based samples. To study magnetic correlations in graphene, we systematically carry out quantum Monte Carlo simulations of the Hubbard model on a honeycomb lattice. In the filling region below the Van Hove singularity, the system shows a short-range ferromagnetic correlation, which is slightly strengthened by the on-site Coulomb interaction and markedly by the next-nearest-neighbor hopping integral. The ferromagnetic properties depend on the electron filling strongly, which

may be manipulated by the electric gate. Due to its resultant high controllability of ferromagnetism, graphene-based samples may facilitate the new development of many applications.

In the chapter 5, we examined theoretically the magnetism of impurity adatoms in graphene by quantum Monte Carlo simulation technique based on Hirsch-Fye algorithm. When tuning the Fermi energy of graphene by gate voltage with available experiments, the values of occupancy and local moment for impurity can be changed. Furthermore, with medium and large hybridizations between impurity and graphene atoms, the local moment can be switched on and off by Kondo effects. We also use maximum entropy method to study the spectral density from Green's function for impurity, and we find very unconventional behaviors which are absolutely different from the cases in the normal metal. These signatures of spectral density enlarge the possibility for controlling the impurity magnetism by gate voltage.

# 摘要

本論文主要研究了三個強關聯阻錯體系：雙層三角晶格中的赫伯德(Hubbard)模型，這個系統對應 $Na_xCoO_2 \cdot yH_2O$ 材料；二維石墨層(graphene)中電子的行爲；二維石墨層中的安德森(Anderson) 雜質。本文主要的數值方法是行列式量子門特卡洛方法(determinant quantum Monte Carlo method)，論文的第二章將詳細介紹此方法。

第三章，我們研究了赫伯德模型在兩類雙層三角晶格中的鉄磁漲落。我們首先從緊束縛(tight-binding)模型出發，研究了兩類三角晶格的能譜，態密度，自旋磁化率。然後考慮了庫倫相互作用的效應，分別運用了無規相近似(random phase approximation) 方法和行列式量子門特卡洛方法計算了兩類三角晶格系統的自旋磁化率，並且進行比較了，重點考察了層間耦合係數的效應。

第四章，我們主要討論了二維石墨層中的鉄磁性質。爲了具體研究這一性質，我們在六角晶格上對單帶赫伯德模型進行了量子門特卡洛數值模擬。儅電子的佔據數處於範霍伕奇點(Van Hove singularity)附近時，系統有短程的鉄磁關聯，並且這種關聯隨著電子間的相互作用和晶格的次近鄰躍遷矩陣元的增加而顯著加強。由於二維石墨層中的鉄磁性質和電子的佔據數有這種比較強的依賴關係，並且電子的佔據數可以通過外電場門電壓來調節，所以在二維石墨層中可以獲得可調節的鉄磁關聯，由此可以發展這種材料技術上的實際應用。

第五章，在二維石墨層表面，我們運用量子門特卡洛方法具體研究了安德森雜質問題。儅依靠外電場調節體系的費米能級的時候，雜質原子的電子佔據數和磁矩可以得到控制，進一步通過對於近籐效應(Kondo effect) 的研究，我們發現原子的磁矩可以通過外電場來打開或者關閉。我們還運用了最大熵(maximum entropy) 方法從雜質原子的格林函數得到了譜密度，並且發現了一些非常有別于雜質在正常金屬中的一些性質。這些性質有利於我們利用實驗手段來控制雜質原子的磁性。

# Acknowledgement

I would like to thank my supervisor Prof. Hai-Qing Lin.

I would like to thank my collaborators: Prof. Zhong-Bing Huang, Prof. J. E. Gubernatis, Dr. Shi-Quan Su, and Tianxing Ma.

I would like to thank Prof. Shijian Gu, Prof. Ligang Wang, Prof. Junpeng Cao, Prof. Yi Zhou and Prof. Yanling Li.

I would like to thank my friends: Ting Chen, Yang Liu, Lei Sun, Bobo Wei, Haiping Yin, Nan Zhao and D. Long.

I would like to thank my parents and my sisters.

# Contents

# List of Figures

# List of Tables

# Chapter 1

# Introduction

In this research thesis we mainly examine magnetic states of three strongly correlated systems by quantum Monte Carlo (QMC) simulation. The following issues will be addressed in this thesis: magnetic properties of bilayer triangular lattice, ferromagnetism in graphene and magnetic impurity in graphene. In the first two projects, we focus on the effects of geometrical frustrations on magnetic correlations in the bilayer triangular lattice and graphene system (honeycomb lattice). The two systems have similar lattice structures: the interlayer and intralayer bonds

of bilayer triangular lattice correspond to nearest-neighbor and next-nearest-neighbor bonds of graphene, respectively. We find that their underlying physics are the same: the large density of states of electrons on the Fermi surface reduced by the geometrical frustration drives the magnetic correlations in these systems. In the last project, we transfer our attention from the magnetic state of graphene itself to that of an impurity atom in graphene system, and due to its unusual electronic excitations described in terms of massless fermions, the Kondo effect of impurity becomes tunable through changing Fermi energy by an electric field, which is significant for graphene as a candidate of spintronics device.

In the chapter 3, we begin to study the magnetic properties of bilayer triangular lattice within Hubbard model, which is a highly frustrated system. Because of recent discovery of superconductivity in $Na_xCoO_2 \cdot yH_2O$ [1], and related fascinating normal state properties [2, 3, 4] have revived people's

interests in geometrically frustrated systems, such as triangular layers. Although the single-band Hubbard model has been widely studied and understood, it can still be used as the minimum theoretical model when we investigate electron correlations on the two-dimensional triangular lattice. As a starting point, the single-band Hubbard model also helps us study the mechanisms of magnetic fluctuations and superconductivity induced by electron-electron interactions. Previously, the Hubbard model on the single-layer triangular lattice has been studied with various techniques: such as the one-loop renormalization-group [5] and the fluctuation exchange approaches.[6] Antiferromagnetic correlations near the half filling and ferromagnetic fluctuations near the Van Hove singularity (VHS) were studied by the determinant quantum Monte Carlo (DQMC) and constrain path Monte Carlo (CPMC) methods, respectively [7, 8].

$Na_xCoO_2 \cdot yH_2O$ has a multilayer structure, and in this system, the distance and couplings between the two $CoO_2$ layers de-

pend on the inserted $H_2O$ molecules, which are of great interest from both a chemical and physical point of view [9, 10, 11, 12]. They are also key to understand the pairing mechanism. To address the influences of $H_2O$ molecules between the two $CoO_2$ layers, it is worth the effort to study the single-band Hubbard model on the bilayer triangular lattices. Previously, electronic structures of cobalt oxide bilayer-hydrate were studied by the first-principles calculations [13]. Quantum phase transition was also discussed in the content of the Heisenberg model on the bilayer triangular lattices [14]. For related researches, there are studies of the single-band Hubbard model on bilayer square lattices [15, 16].

In reality, many materials discuss the structures of bilayer triangular lattice. For example, spin-dimer materials $Ba_3Mn_2O_8$ [17, 18, 19] and $Mn_6$ molecules [20], where Mn ions form the bilayer triangular lattice. Another interesting material is graphene, which has attracted great attention recently due to its Dirac

fermionic behavior at low energy [21]. Graphene has honeycomb lattice, which can be regarded as two interpenetrating triangular sublattices, and it is similar to the bilayer triangular lattices we are interested in. Here, interlayer coupling plays an important role in these systems.

Metallic ferromagnetism (FM) in correlated systems is a long-standing issue which has been actively studied both numerically and analytically [22, 23, 24, 25]. It has been quite well known that the geometry of the system, the shape of the density of states(DOS), and the large degeneracy of single-particle energy level are crucial to the stability of the ferromagnetic state [26, 27, 28]. The triangular lattice, compared to square lattice, has a higher degeneracy on the energy level and asymmetric distribution of the DOS, so it favors stronger ferromagnetic fluctuation in some parameter regions. For the single-layer triangular lattice, its DOS has one VHS at band filling $\langle n \rangle = 1.5$. When the interlayer hopping $t'$ is introduced, two VHS appear with DOS

decreasing(see below). According to the itinerant electron FM theory, the ferromagnetic fluctuations tend to the higher DOS on the Fermi surface. So the interlayer hopping $t'$ will influence the ferromagnetic fluctuations, which motivates us to compare the spin susceptibilities of single-layer with bilayer triangular lattices.

The search for high temperature ferromagnetic semiconductors, which combine the properties of FM and semiconductors and allow for practical applications of spintronics, has evolved into a broad field of materials science[29, 30]. Scientists require a material in which the generation, injection, and detection of spin-polarized electrons is accomplished without strong magnetic fields, with processes effective at or above room temperature[31]. Although some of these requirements have been successfully demonstrated, most semiconductor-based spintronics devices are still at the proposal stage since useful ferromagnetic semiconductors have yet to be developed[32]. Recently, scientists anticipate

that graphene-based electronics may supplement silicon-based technology, which is nearing its limits[21, 33, 34]. Unlike silicon, the single layer graphene is a zero-gap two-dimensional (2D) semiconductor, and the bilayer graphene provides the first semiconductor with a gap that can be tuned externally[35]. Graphene exhibits gate-voltage controlled carrier conduction, high field-effect mobility, and a small spin-orbit coupling, making it a very promising candidate for spintronics application [36, 37]. In view of these characteristics, the study of the high controllability of FM in graphene-based samples is of fundamental and technological importance, since it increases the possibility of using graphene in spintronics and other applications, which motivates us to research FM in graphene system in the chapter 4.

On the other hand, the existence of FM in graphene is an unresolved issue. Many believe that both the electron-electron correlations and DOS at the Fermi surface in solids play es-

sential roles in determining FM behaviors. This conclusion also applies to graphene. Recent experimental and theoretical results in graphene[38, 39, 40, 41, 42, 43, 44] show that the electron-electron interactions must be taken into account in order to obtain a fully consistent picture of graphene. The honeycomb structure of graphene exhibits VHS in the DOS, which may result in strong ferromagnetic fluctuations, as demonstrated by recent QMC simulations of the Hubbard model on the square and triangular lattices [45, 8, 46]. After taking both electron-electron interaction and lattice structure into consideration, the bidimensional Hubbard model on the honeycomb lattice[47, 48, 49, 50, 51] is a good candidate to study FM behaviors in graphene. Early studies of the bidimensional Hubbard model on the honeycomb lattice were based on mean field approximations and the perturbation theory[51]. However, the results obtained are still actively debated because they are very sensitive to the approximation used. As such, exact numerical results are highly

desirable for they provide unbias information and would serve as useful bench marks for analytical approach. Therefore, we use the DQMC simulation technique[52] to investigate the nature of magnetic correlation in the presence of moderate Coulomb interactions on the honeycomb lattice. We are particularly interested in the low filling case where strong ferromagnetic fluctuation exists according to our data. We also study ferromagnetic fluctuations as functions of the electron filling, because the application of local gate techniques enables us to modulate electron filling[21, 33], which is the first step on the road towards graphene-based electronics.

In the chapter 5, we address the problem of graphene coupling with magnetic impurity atom and show that the peculiar electronic properties of graphene system lead to some interesting new effects. Firstly, due to a massless Dirac-like spectrum for conduction electrons in graphene, the system can exhibit unconventional Kondo behaviors and the Kondo temperature

becomes very low near Dirac point. Secondly, through using a electric field, the screening of impurity local moment from conduction electrons can be controlled by changing Fermi energy, and furthermore, under some conditions, the local moment can be switched on and off. Thirdly, we calculate the spectral density of impurity using maximum entropy method, the behaviors of spectral density are absolutely different from that in normal metal.

The impurity problem in graphene has been studied by perturbation theory, mean-field method, and numerical renormalization group [53, 54, 55]. In our research work, we use DQMC method based on HF algorithm which is powerful tool without sign problem at low temperature. And when studying the Kondo effect, we pay more attention on the chemical potential of graphene, which is more interesting experimentally.

---

□ **End of chapter.**

# Chapter 2

# Numerical Method

## 2.1 Determinant Quantum Monte Carlo Method Based on BSS Algorithm

In this section, we introduce the determinant quantum Monte Carlo method (QMC) based on Blankenbecler-Scalapino-Sugar (BSS) algorithm [52]. We mainly present the scheme of this numerical method following the paper of reference[56]. To deal with systems of many interacting fermions, one is generally interested in their collective properties, which are well described within the theory of Statistical Mechanics. Typical questions

about a system are related to its magnetic property, to its charge distribution, and to whether it is insulating, metallic, or superconductor. The simplest theoretical model describing interacting fermions on a lattice is the single-band Hubbard model [57], which is defined by the Hamiltonian as

$$H = -t \sum_{\langle \mathbf{i},\mathbf{j}\rangle,\sigma} \left( c^{\dagger}_{\mathbf{i}\sigma} c_{\mathbf{j}\sigma} + \text{H.c.} \right) + U \sum_{\mathbf{i}} n_{\mathbf{i}\uparrow} n_{\mathbf{i}\downarrow} - \\ -\mu \sum_{\mathbf{i}} \left( n_{\mathbf{i}\uparrow} + n_{\mathbf{i}\downarrow} \right), \tag{2.1}$$

where $t$ is the hopping integral, $U$ is the on-site Coulomb interaction, $\mu$ is the chemical potential controlling the fermion filling, and $\mathbf{i}$ denotes site for a $d$-dimensional lattice; we consider nearest-neighbor hopping only, as denoted by $\langle \ldots \rangle$. The operators $c^{\dagger}_{\mathbf{i}\sigma}$ and $c_{\mathbf{i}\sigma}$ respectively create and annihilate a fermion with spin $\sigma$ on the (single) orbital centred at $\mathbf{i}$, while $n_{\mathbf{i}\sigma} \equiv c^{\dagger}_{\mathbf{i}\sigma} c_{\mathbf{i}\sigma}$. The Hubbard model describes the competition between opposing tendencies of itinerancy (driven by the hopping term), and localization (driven by the on-site repulsion).

The Hubbard model only can be exactly solved in the case of one-dimension sytem, through the Bethe ansatz; while correlation functions are not directly available. In higher dimensions approximation schemes have to be used, and numerical techniques such as QMC simulations have proven to be crucial in obtaining information about strongly correlated fermions. Here we focus on the actual details of the grand-canonical formulation with auxiliary fields leading to fermionic determinants.

For the Hubbard model, the Coulomb interaction and hopping terms do not commute with each other, and, in addition, hopping terms involving the same site also do not commute with each other. Therefore, when calculating the grand partition function,

$$\mathcal{Z} = \mathcal{T}r\ e^{-\beta H}, \tag{2.2}$$

where $\mathcal{T}r$ stands for a sum over all numbers of particles and over all site occupations, one must cast the quartic term into a bilinear form. We separate the exponentials with the Suzuki-

Trotter decomposition scheme [58], which is based on the fact that

$$e^{\Delta\tau(H_0+H_I)} = e^{\Delta\tau H_0}e^{\Delta\tau H_I} + \mathcal{O}\left[(\Delta\tau)^2\left[H_0, H_I\right]\right], \qquad (2.3)$$

for $H_0$ and $H_I$ generic non-commuting operators. Calling $H_0$ and $H_I$, respectively the bilinear and quartic terms in the Hubbard Hamiltonian, we introduce a small parameter $\Delta\tau$ through $\beta = M\,\Delta\tau$, and apply the Suzuki-Trotter formula as

$$\begin{aligned} e^{-\beta(H_0+H_I)} &= \left(e^{\Delta\tau H_0+\Delta\tau H_I}\right)^M = \\ &= \left(e^{\Delta\tau H_0}e^{\Delta\tau H_I}\right)^M + \mathcal{O}\left[(\Delta\tau)^2 U\right]. \end{aligned} \qquad (2.4)$$

The analogy with the path integral formulation of Quantum Mechanics suggests that the above procedure amounts to the imaginary-time interval $(0, \beta)$ being discretized into $M$ slices separated by the interval $\Delta\tau$. It is clear that from Eq. (2.4), the finiteness of $\Delta\tau$ is also a source of systematic errors; these errors can be downsized by obtaining estimates for successively smaller values of $\Delta\tau$.

Table 2.1: Determining parameter $\lambda$ in HS transformation

| $n_\uparrow$ | $n_\downarrow$ | $m$ | $n$ | $\frac{1}{2}e^{-\frac{U\Delta\tau}{2}n}\sum_{s=\pm1}e^{-s\lambda m}$ | $e^{-U\Delta\tau n_\uparrow n_\downarrow}$ |
|---|---|---|---|---|---|
| 1 | 0 | 1 | 1 | $e^{-U\Delta\tau}\cosh(\lambda)$ | 1 |
| 0 | 1 | −1 | 1 | $e^{-U\Delta\tau}\cosh(\lambda)$ | 1 |
| 1 | 1 | 0 | 2 | $e^{-U\Delta\tau}$ | $e^{-U\Delta\tau}$ |
| 0 | 0 | 0 | 1 | 1 | 1 |

Having separated the exponentials, we can now decouple the quartic terms in $H_I$ by the Hubbard-Stratonovich (HS) transformation,

$$\begin{aligned} e^{-U\Delta\tau n_\uparrow n_\downarrow} &= \frac{1}{2}e^{-\frac{U\Delta\tau}{2}n}\sum_{s=\pm1}e^{-s\lambda m} = \\ &= \frac{1}{2}\sum_{s=\pm1}\prod_{\sigma=\uparrow,\downarrow}e^{-\left(\sigma s\lambda+\frac{U\Delta\tau}{2}\right)n_\sigma}, \quad U>0, \end{aligned} \tag{2.5}$$

where $n \equiv n_\uparrow + n_\downarrow$, $m \equiv n_\uparrow - n_\downarrow$ and we can use the Table (2.1) to determine the parameter $\lambda$.

$$\cosh(\lambda) = e^{|U|\Delta\tau/2}. \tag{2.6}$$

Here, we see that, by HS transformation, we decouple quartic terms but at the cost of introducing a auxiliary field $s$ at every site and time slice.

We now replace the on-site interaction on every site of the space-time lattice by Eqs. (2.5), leading to the sought form in which only bilinear terms appear in the exponential. We get

$$\mathcal{Z} = \left(\frac{1}{2}\right)^{L^d M} \operatorname*{Tr}_{\{s\}} \mathcal{T}r \prod_{\ell=M}^{1} \prod_{\sigma=\uparrow,\downarrow} e^{-\Delta\tau \sum_{i,j} c^{\dagger}_{i\sigma}(H_0)_{ij} c_{j\sigma}} e^{-\Delta\tau \sum_i c^{\dagger}_{i\sigma} V_i^{\sigma}(\ell) c_{i\sigma}}, \tag{2.7}$$

where the traces are over auxiliary fields and over fermion occupancies on every site, and the product from $\ell = M$ to 1 simply reflects the fact that earlier 'times' appear to the right. The time-slice index $\ell$ appears through the HS field $s_i(\ell)$ in

$$V_i^{\sigma}(\ell) = \frac{1}{\Delta\tau}\lambda\sigma s_i(\ell) + \left(\mu - \frac{U}{2}\right), \tag{2.8}$$

which are the elements of the $N_s \times N_s$ diagonal matrix $\mathsf{V}^{\sigma}(\ell)$; here, $N_s$ is the number of the lattice site. One also needs the

$N_s \times N_s$ hopping matrix $H_0$, with elements

$$(H_0)_{ij} = \begin{cases} -t & \text{if } i \text{ and } j \text{ are nearest neighbors,} \\ 0 & \text{otherwise} \end{cases} \tag{2.9}$$

With bilinear forms in the exponential, the fermions can be traced out of Eq. (2.7), we have [56]

$$\mathcal{Z} = \left(\frac{1}{2}\right)^{L^d M} \operatorname*{Tr}_{\{s\}} \prod_{\sigma} \det\left[\mathbf{1} + \mathsf{B}_M^\sigma \mathsf{B}_{M-1}^\sigma \ldots \mathsf{B}_1^\sigma\right], \tag{2.10}$$

where we have defined

$$\mathsf{B}_\ell^\sigma \equiv e^{-\Delta\tau H_0} e^{-\Delta\tau \mathsf{V}^\sigma(\ell)}, \tag{2.11}$$

in which the dependence with the auxiliary field has not been explicitly written, but should be understood, since they come in through the matrix $\mathsf{V}^\sigma(\ell)$. Introducing

$$\mathsf{O}^\sigma(\{s\}) \equiv 1 + \mathsf{B}_M^\sigma \mathsf{B}_{M-1}^\sigma \ldots \mathsf{B}_1^\sigma, \tag{2.12}$$

we arrive at

$$\begin{aligned} \mathcal{Z} &= \left(\frac{1}{2}\right)^{L^d M} \operatorname*{Tr}_{\{s\}} \det \mathsf{O}^\uparrow(\{s\}) \cdot \det \mathsf{O}^\downarrow(\{s\}) = \\ &= \operatorname*{Tr}_{\{s\}} \rho(\{s\}), \end{aligned} \tag{2.13}$$

where the last equality defines an effective 'density matrix', $\rho(\{s\})$.

And, finally, we must discuss the calculation of average values. For two operators $c_{i\sigma}$ and $c^{\dagger}_{j\sigma}$, the equal-'time' Green's function is defined as

$$\langle c_{i\sigma} c^{\dagger}_{j\sigma} \rangle = \frac{1}{\mathcal{Z}} \mathrm{Tr}_{\{s\}} \mathcal{T}r \left[ c_{i\sigma} c^{\dagger}_{j\sigma} \prod_{\ell\sigma} e^{-\Delta\tau H_0} e^{-\Delta\tau V^{\sigma}(\ell)} \right]. \qquad (2.14)$$

If we now define the fermion average – or Green's function – for a given configuration of the HS fields as

$$\langle c_{i\sigma} c^{\dagger}_{j\sigma} \rangle_{\{s\}} \equiv \frac{1}{\rho(\{s\})} \mathcal{T}r \left[ c_{i\sigma} c^{\dagger}_{j\sigma} \prod_{\ell\sigma} e^{-\Delta\tau H_0} e^{-\Delta\tau V^{\sigma}(\ell)} \right], \qquad (2.15)$$

the Green's function becomes

$$\langle c_{i\sigma} c^{\dagger}_{j\sigma} \rangle = \frac{1}{\mathcal{Z}} \mathrm{Tr}_{\{s\}} \langle c_{i\sigma} c^{\dagger}_{j\sigma} \rangle_{\{s\}} \rho(\{s\}). \qquad (2.16)$$

At this point it should be stressed the important role played by the Green's functions in the simulations. Firstly, according to Eq. (2.16), the average value of an operator is straighforwardly obtained by sampling the corresponding Green's function over

the HS configurations weighted by $\rho(\{s\})$. Secondly, as it will become apparent in process of simulation, the single particle Green's function, $\langle c_{\mathbf{i}\sigma} c^{\dagger}_{\mathbf{j}\sigma} \rangle_{\{s\}}$, plays a central role in the updating process itself. Through applying linear transformation we obtain this quantity as the element $\mathbf{ij}$ of an $N_s \times N_s$ matrix [59, 60]:

$$\langle c_{\mathbf{i}\sigma} c^{\dagger}_{\mathbf{j}\sigma} \rangle_{\{s\}} = \left[ \left( 1 + \mathsf{B}^{\sigma}_{M} \mathsf{B}^{\sigma}_{M-1} \ldots \mathsf{B}^{\sigma}_{1} \right)^{-1} \right]_{\mathbf{ij}}, \tag{2.17}$$

which is a suitable form for numerical calculations. And, thirdly, within the present approach the fermions only interact with the auxiliary fields, so that Wick's theorem[61] holds for a fixed HS configuration[59, 60, 62]; the two-particle Green's functions are then readily given in terms of the single-particle ones as

$$\begin{aligned} \langle c^{\dagger}_{i_1} c_{i_2} c^{\dagger}_{i_3} c_{i_4} \rangle_{\{s\}} &= \langle c^{\dagger}_{i_1} c_{i_2} \rangle_{\{s\}} \langle c^{\dagger}_{i_3} c_{i_4} \rangle_{\{s\}} + \\ &+ \langle c^{\dagger}_{i_1} c_{i_4} \rangle_{\{s\}} \langle c_{i_2} c^{\dagger}_{i_3} \rangle_{\{s\}}, \end{aligned} \tag{2.18}$$

where the indices include spin, but since the $\uparrow$ and $\downarrow$ spin channels are factorized [*c.f.* Eq. (2.15)], these fermion averages are zero if the spins are different. All average values of interest are

therefore calculated in terms of single-particle Green's functions.

As will be seen, unequal-time correlation functions are also important. We define the operator in the 'Heisenberg picture' as

$$c_{i\sigma}(\ell) \equiv c_{i\sigma}(\tau) = e^{\tau\mathcal{H}}\, c_{i\sigma}\, e^{-\tau\mathcal{H}},\ \tau \equiv \ell\Delta\tau, \tag{2.19}$$

so that the initial time is set to $\tau = \Delta\tau$ with this discretization, and $c^{\dagger}_{i\sigma}(\ell) \neq [c_{i\sigma}(\ell)]^{\dagger}$. We show that the unequal-time Green's function, for $\ell_1 > \ell_2$, is given by [59]

$$\begin{aligned} G^{\sigma}_{ij}(\ell_1;\ell_2) &\equiv \langle c_{i\sigma}(\ell_1) c^{\dagger}_{j\sigma}(\ell_2)\rangle_{\{s\}} = \\ &= \left[\mathsf{B}^{\sigma}_{\ell_1}\mathsf{B}^{\sigma}_{\ell_1-1}\ldots\mathsf{B}^{\sigma}_{\ell_2+1}\,\mathsf{g}^{\sigma}(\ell_2+1)\right]_{ij}, \end{aligned} \tag{2.20}$$

in which the Green's function matrix at the $\ell$-th time slice is defined as

$$\mathsf{g}^{\sigma}(\ell) \equiv [1 + \mathsf{A}^{\sigma}(\ell)]^{-1}, \tag{2.21}$$

with

$$\mathsf{A}^{\sigma}(\ell) \equiv \mathsf{B}^{\sigma}_{\ell-1}\mathsf{B}^{\sigma}_{\ell-2}\ldots\mathsf{B}^{\sigma}_{1}\mathsf{B}^{\sigma}_{M}\ldots\mathsf{B}^{\sigma}_{\ell}. \tag{2.22}$$

We notice the order in which the products of B's are taken

in Eqs. (2.17), (2.20), and (2.22); in Eq. (2.20), in particular, the product runs from $\ell_2 + 1$ to $\ell_1$, and not cyclically as in Eq. (2.22). Also, for a given configuration $\{s\}$ of the HS spins, the equal-time Green's functions do display a time-slice dependence, as expressed by Eq. (2.21); they only become (approximately) equal after averaging over a large number of configurations.

The QMC simulations is in the process of sweeping through a space-time lattice. With the parameters of the Hamiltonian, $U$ and $\mu$, as well as the temperature, fixed from the outset, we begin by generating, say a random configuration, $\{s\}$, for the HS fields. Since the walker starts on the first time-slice, we use the definition, Eq. (2.17), to calculate the Green's function at $\ell = 1$. As the walker sweeps the spatial lattice, it attempts to flip the HS spin at every one of the $N_s$ points.

At this point, it is convenient to picture the walker attempting to flip the HS (Ising) spin on a generic site, $\mathbf{i}$ of a generic time slice, $\ell$. If the spin is flipped, the matrices $\mathsf{B}_\ell^\uparrow$ and $\mathsf{B}_\ell^\downarrow$ change due

to the element **ii** of the matrices $\mathsf{V}^{\uparrow}(\ell)$ and $\mathsf{V}^{\downarrow}(\ell)$, respectively, being affected; see Eqs. (2.8) and (2.11). The expression for the change in the matrix element, as $s_{\mathbf{i}}(\ell) \to -s_{\mathbf{i}}(\ell)$, is

$$\delta V^{\sigma}_{\mathbf{ij}}(\ell) \equiv V^{\sigma}_{\mathbf{ij}}(\ell, -s) - V^{\sigma}_{\mathbf{ij}}(\ell, s) = -2\lambda\sigma s_{\mathbf{i}}(\ell)\ \delta_{\mathbf{ij}}, \tag{2.23}$$

which allows us to write the change in $\mathsf{B}^{\sigma}_{\ell}$ as a matrix product,

$$\mathsf{B}^{\sigma}_{\ell} \to [\mathsf{B}^{\sigma}_{\ell}]' = \mathsf{B}^{\sigma}_{\ell}\Delta^{\sigma}_{\ell}(\mathbf{i}), \tag{2.24}$$

where the elements of the matrix $\Delta^{\sigma}_{\ell}(\mathbf{i})$ are

$$[\Delta^{\sigma}_{\ell}(\mathbf{i})]_{\mathbf{jk}} = \begin{cases} 0 & \text{if } \mathbf{j} \neq \mathbf{k}, \\ 1 & \text{if } \mathbf{j} = \mathbf{k} \neq \mathbf{i}, \\ e^{-2\lambda\sigma s_{\mathbf{i}}(\ell)} & \text{if } \mathbf{j} = \mathbf{k} = \mathbf{i}. \end{cases} \tag{2.25}$$

Let us now call $\{s\}'$ and $\{s\}$, the HS configurations in which all Ising spins are the same, except for those on site $(\mathbf{i}, \ell)$, which are opposite. We can then write the ratio of 'Boltzmann weights' as

$$r' = \frac{\rho\left(\{s\}'\right)}{\rho\left(\{s\}\right)} = \frac{\det \mathsf{O}^{\uparrow}\left(\{s\}'\right) \cdot \det \mathsf{O}^{\downarrow}\left(\{s\}'\right)}{\det \mathsf{O}^{\uparrow}\left(\{s\}\right) \cdot \det \mathsf{O}^{\downarrow}\left(\{s\}\right)} = R_{\uparrow}R_{\downarrow}, \tag{2.26}$$

where we have defined the ratio of fermion determinants as

$$R_\sigma \equiv \frac{\det \mathsf{O}^\sigma\left(\{s\}'\right)}{\det \mathsf{O}^\sigma\left(\{s\}\right)}. \tag{2.27}$$

It is important to notice that one actually does not need to calculate determinants, since $R_\sigma$ is given in terms of the Green's function:

$$\begin{aligned} R_\sigma &= \frac{\det\left[1+\mathsf{A}^\sigma(\ell)\Delta_\ell^\sigma(\mathbf{i})\right]}{\det\left[1+\mathsf{A}^\sigma(\ell)\right]} = \\ &= \det\left[\left(1+\mathsf{A}^\sigma(\ell)\Delta_\ell^\sigma(\mathbf{i})\right)\mathsf{g}^\sigma(\ell)\right] = \\ &= \det\left[1+\left(1-\mathsf{g}^\sigma(\ell)\right)\left(\Delta_\ell^\sigma(\mathbf{i})-1\right)\right] = \\ &= 1+\left(1-\mathsf{g}_{\mathbf{ii}}^\sigma(\ell)\right)\left(e^{-2\lambda\sigma s_{\mathbf{i}}(\ell)}-1\right). \end{aligned} \tag{2.28}$$

The last equality follows from the fact that

$$\Gamma_\ell^\sigma(\mathbf{i}) \equiv \Delta_\ell^\sigma(\mathbf{i}) - 1 \tag{2.29}$$

is a matrix such that all elements are zero, except for the $\mathbf{i}$-th position in the diagonal, which is $\gamma_\ell^\sigma(\mathbf{i}) \equiv e^{-2\lambda\sigma s_{\mathbf{i}}(\ell)} - 1$. With this simple form for $r' = R_\uparrow R_\downarrow$, we can adopt the *heat-bath algorithm*[63] is then easily implemented, with the probability

of acceptance of the new configuration $r$ being given by

$$r = \frac{r'}{1 + r'} \tag{2.30}$$

Eq. (2.30), with Eqs. (2.26) and (2.28). We compare the probability $r$ with a random number, and if $r$ is larger than the random number the flip is accepted. Alternatively[64], we can use *Metropolis algorithm*, in the meantime the probability is $r = r'$. If $r' > 1$, the flip is accepted; while $r' < 1$ we continue to compare $r'$ with a random number if it is larger than this number the flip is still accepted.

If the flip is accepted, the whole Green's function for the current time slice must be updated; this is the non-local aspect of QMC simulations we referred to earlier. There are two method for updating the Green's function. One can either compute the 'new' one from scratch, through Eq. (2.21), or iterate the 'old' Green's function, by following along the lines that led to Eq.

(2.28), which yields

$$\bar{\mathbf{g}}^{\sigma}(\ell) = \left[1 + \left(1 - \mathbf{g}^{\sigma}(\ell)\right)\Gamma^{\sigma}_{\ell}(\mathbf{i})\right]^{-1} \mathbf{g}^{\sigma}(\ell). \tag{2.31}$$

An explicit form for $\bar{\mathbf{g}}^{\sigma}(\ell)$ is obtained, and we see that the sparse matrix of $\mathcal{U}^{\sigma} \equiv 1 + \left(1 - \mathbf{g}^{\sigma}(\ell)\right)\Gamma^{\sigma}_{\ell}(\mathbf{i})$ has the formula as

$$\mathcal{U}^{\sigma} = \begin{pmatrix} 1 & 0 & 0 & \cdots & 0 & 0 \\ 0 & 1 & 0 & \cdots & 0 & 0 \\ \vdots & \vdots & \vdots & \vdots & \vdots & \vdots \\ 0 & \cdots & 0 & 1 + \left[1 - \mathbf{g}^{\sigma}(\ell)\right]_{\mathbf{ii}}\Gamma^{\sigma}_{\ell}(\mathbf{i}) & \cdots & 0 \\ \vdots & \vdots & \vdots & \vdots & \vdots & \vdots \\ 0 & 0 & \cdots & 0 & 0 & 1 \end{pmatrix}. \tag{2.32}$$

It is easy to calculate the inverse of this sparse matrix

$$\left[1 + \left(1 - \mathbf{g}^{\sigma}(\ell)\right)\Gamma^{\sigma}_{\ell}(\mathbf{i})\right]^{-1} = 1 - \frac{1}{R_{\sigma}}\left(1 - \mathbf{g}^{\sigma}(\ell)\right)\Gamma^{\sigma}_{\ell}(\mathbf{i}) \tag{2.33}$$

with $R_{\sigma}$ being given by Eq. (2.28). The element $\mathbf{jk}$ of the Green's function is then updated according to

$$\bar{g}^{\sigma}_{\mathbf{jk}}(\ell) = g^{\sigma}_{\mathbf{jk}}(\ell) - \frac{\left[\delta_{\mathbf{ji}} - g^{\sigma}_{\mathbf{ji}}(\ell)\right]\gamma^{\sigma}_{\ell}(\mathbf{i})\, g^{\sigma}_{\mathbf{ik}}(\ell)}{1 + \left[1 - g^{\sigma}_{\mathbf{ii}}(\ell)\right]\gamma^{\sigma}_{\ell}(\mathbf{i})}. \tag{2.34}$$

Alternatively, one could arrive at the same result by solving a Dyson's equation for $\bar{g}^{\sigma}_{\mathbf{jk}}(\ell)$ [60].

After the walker tries to flip the spin on the last site of the $\ell$-th time slice, it moves on to the first site of the $(\ell+1)$-th time slice. We therefore need the Green's function for the $(\ell+1)$-th time slice, which, as before, can be calculated either from scratch, or iteratively from the Green's function for the $\ell$-th time slice. Indeed, by comparing $[\mathsf{g}^{\sigma}(\ell+1)]^{-1}$ with $[\mathsf{g}^{\sigma}(\ell)]^{-1}$, as given by Eq. (2.21), it is easy to see that

$$\mathsf{g}^{\sigma}(\ell+1) = \mathsf{B}^{\sigma}_{\ell}\mathsf{g}^{\sigma}(\ell)\left[\mathsf{B}^{\sigma}_{\ell}\right]^{-1}, \tag{2.35}$$

which can be used to compute the Green's function in the subsequent time slice.

## 2.2 Determinant Quantum Monte Carlo Method Based on HF Algorithm

In this section, we discuss the DQMC based on Hirsch-Fye (HF) algorithm which is a powerful method to deal with Anderson impurity model [65]. At low temperature it avoids negative-sign problem and numerical instabilities. The Anderson impurity model has the formula as

$$\begin{aligned} H &= \sum_{k,\sigma} \epsilon_k c^\dagger_{k\sigma} c_{k\sigma} + \sum_{k,\sigma} (V_k c^\dagger_{k\sigma} d_\sigma + \text{H.c.}) + \epsilon_d \sum_\sigma n_{d\sigma} + U n_{d\uparrow} n_{d\downarrow} \\ &\equiv H_0 + H_I \end{aligned} \tag{2.36}$$

here, $c_{k\sigma}$ and $c^\dagger_{k\sigma}$ are operators of conduction electrons in host metal, and, $d^\dagger_\sigma$ and $d_\sigma$ are the operators of impurity. We also divide the total Hamiltonian into two parts: $H_0$ is the part of bilinear terms and $H_I$ is the part of Coulomb interaction for impurity orbital. So the partition function has the formula as

$$\mathcal{Z} = \mathcal{T}r e^{-\beta H} = \mathcal{T}r \prod_{\ell=M}^{1} e^{-\Delta\tau H} \cong \mathcal{T}r \prod_{\ell=M}^{1} e^{-\Delta\tau H_0} e^{-\Delta\tau H_I}, \tag{2.37}$$

here, $\beta = M\Delta\tau$,and as Eq. (2.5)

$$e^{-U\Delta\tau n_\uparrow n_\downarrow} = \frac{1}{2}\sum_{s=\pm 1}\prod_{\sigma=\uparrow,\downarrow} e^{-\left(\sigma s\lambda + \frac{U\Delta\tau}{2}\right)n_\sigma}, \tag{2.38}$$

and $\cosh(\lambda) = e^{\Delta\tau U/2}$. Taking the trace over fermion degrees of freedom, the partition function can be written as

$$\mathcal{Z} = \operatorname*{Tr}_{\{s\}}\prod_{\sigma=\uparrow,\downarrow}\det_{N_s,M}\mathsf{O}^\sigma(\{s(\ell)\}), \tag{2.39}$$

where $\mathsf{O}^\sigma$ is an $N_sM \times N_sM$ matrix, with $N_s$ the number of spatial sites (or $k$ vectors) for the conduction electrons plus 1 (the impurity orbital). Here we use block matrix to represent the spatial-time matrix $\mathsf{O}^\sigma$, we can see that

$$\begin{aligned}(\mathsf{O}^\sigma)_{\ell,\ell} &= 1\\ (\mathsf{O}^\sigma)_{\ell,\ell-1} &= -e^{-\Delta\tau H_0}e^{\mathsf{V}^\sigma(\ell-1)}(1-2\delta_{\ell,1}),\end{aligned} \tag{2.40}$$

and $(\mathsf{O}^\sigma)_{\ell,m} = 0$ otherwise. In Eq. (2.40), $H_0$ is $N_s \times N_s$ hopping matrix and

$$\mathsf{V}^\sigma(\ell) = \lambda\sigma s(\ell)|d\rangle\langle d| \tag{2.41}$$

is a potential acting only at the impurity site. Using $\mathsf{B}_\ell^\sigma$ defined in Eq. (2.11), we see that $\mathsf{O}^\sigma$ has the formula as

$$\mathsf{O}^\sigma = \begin{pmatrix} 1 & 0 & 0 & \cdots & 0 & \mathsf{B}_M^\sigma \\ -\mathsf{B}_1^\sigma & 1 & 0 & \cdots & 0 & 0 \\ 0 & -\mathsf{B}_2^\sigma & 1 & \cdots & 0 & 0 \\ \vdots & \vdots & \vdots & \vdots & \vdots & \vdots \\ 0 & 0 & \cdots & 0 & -\mathsf{B}_{M-1}^\sigma & 1 \end{pmatrix}. \tag{2.42}$$

The Green's function has the similar formula as Eq. (2.17) and Eq. (2.20)

$$G^\sigma = (\mathsf{O}^\sigma)^{-1}, \tag{2.43}$$

which obey the Dyson's equation as Eq. (2.31)

$$\bar{G} = G + (G - 1)(e^{\mathsf{V}'-\mathsf{V}} - 1)\bar{G} \tag{2.44}$$

relating any two spin configurations. And the potential matrix $\mathsf{V}$ is a is a diagonal matrix in space and time. Since $\mathsf{V}$ in Eq. (2.41) only acts on the $d$ site, Eq. (2.44) provides directly an

$M \times M$ matrix equation for the $d$ Green's equation

$$\bar{G}_{dd}(\ell,\ell') = G_{dd}(\ell,\ell')+[G_{dd}(\ell,\ell'')-\delta_{\ell,\ell''}][\exp(V'_{\ell''}-V_{\ell''})-1]\bar{G}_{dd}(\ell'',\ell') \tag{2.45}$$

When we do the QMC simulation in the space-time lattice, the ratio of Boltzmann weight for two different configurations determine whether the flip is accepted or not. In the H-F algorithm, for flipping at $\ell$ time slice, the ratio has the similar formula to that of the BSS algorithm Eq. (2.28)

$$R = 1 + [1 - G_{dd}(\ell,\ell)][\exp(V' - V) - 1]. \tag{2.46}$$

When a flip at $\ell$ time slice is accepted, all components of the $d$ Green's function are updated through the relation

$$\bar{G} = [1 - (G - 1)(e^{V'-V} - 1)]^{-1}G, \tag{2.47}$$

and the inverse of the matrix in Eq. (2.47) has the same formula as Eq. (2.33), so the suitable form for numerical calculation is

$$\begin{aligned}\bar{G}_{dd}(\ell_1,\ell_2) = \; & G_{dd}(\ell_1,\ell_2) + \tfrac{1}{R}[G_{dd}(\ell_1,\ell) - \delta_{\ell_1,\ell}] \\ & \times[\exp(V'_\ell - V_\ell) - 1]G_{dd}(\ell,\ell_2).\end{aligned} \tag{2.48}$$

Initially, Eq. (2.47) is used to obtain $G_{dd}$ from the Green's function for the fields a set equal to zero,

$$G_{dd} = [1 - (G - 1)(e^{\mathsf{V}} - 1)]^{-1} G^0_{dd}, \tag{2.49}$$

here, $G^0_{dd}$ is non-interacting Green's function. To study the spin and charge correlation functions between impurity and conduction electron, we also need to calculate the Green's functions between impurity and conduction electron $G_{id}$ and $G_{di}$, and, Green's function of conduction electrons $G_{ij}$. Firstly, we write the transpose of Eq. (2.44)

$$\bar{G} = G + (\bar{G} - 1)(1 - e^{-\mathsf{V}'+\mathsf{V}})G. \tag{2.50}$$

Secondly, we reduce the Eq. (2.44) and Eq. (2.50) to $M \times M$ submatrix given that $\mathsf{V}$ only acts on $d$ orbital so the Green's functions have the formulas as

$$\begin{aligned} G_{id} &= G^0_{id} + G^0_{id}(e^{\mathsf{V}} - 1)G_{dd} \\ G_{di} &= G^0_{di} + (G_{dd} - 1)(1 - e^{-\mathsf{V}})G^0_{di} \\ G_{ij} &= G^0_{ij} + G^0_{id}(e^{\mathsf{V}} - 1)G_{dj}. \end{aligned} \tag{2.51}$$

When sweeping the auxiliary field, we only needs to calculate the equal-time Green's function of impurity. After finishing walking through the whole imaginary-time lattice, we firstly calculate the impurity Green's functions(equal-time and unequal-time) with a fixed Ising field in terms of Dyson' equation (2.48), and secondly use Eq. (2.51) to calculate the Green's functions related to the conduction electrons.

---

□ **End of chapter.**

# Chapter 3

# Magnetic Properties of Bilayer Triangular Lattice

## 3.1 Introduction

In this work, we study two types of bilayer triangular lattices as shown in Fig. 3.1. In Fig. 3.1(a), for every atom, there are six nearest neighbors in one layer and three next-nearest neighbors in the other layer. This structure is similar to the honeycomb lattice. For the structure shown in Fig. 3.1(b), every atom has only one next-nearest neighbor in the other layer. We call

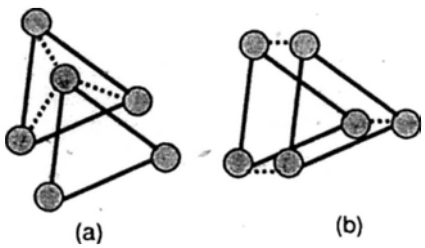


Figure 3.1: (Color online). Two types of bilayer triangular lattices studied in this work are shown as structure A in (a) and structure B in (b).

the lattice shown in Fig. 3.1(a) structure A and in Fig. 3.1(b) structure B in all the followings. These two structures can be regarded as two-dimensional triangular lattices with every unit cell consisting of two atoms. The model Hamiltonian of the system is

$$\begin{aligned} H &= -t \sum_{\langle \mathrm{i,j} \rangle d\sigma} (c^{\dagger}_{\mathrm{j}d\sigma} c_{\mathrm{i}d\sigma} + \mathrm{H.c.}) \\ &\quad -t' \sum_{\langle \mathrm{i,j} \rangle \sigma} (c^{\dagger}_{\mathrm{j}1\sigma} c_{\mathrm{i}2\sigma} + \mathrm{H.c.}) \\ &\quad +U \sum_{\mathrm{i}d} n_{\mathrm{i}d\uparrow} n_{\mathrm{i}d\downarrow} - \mu \sum_{\mathrm{i}d\sigma} n_{\mathrm{i}d\sigma}, \end{aligned} \tag{3.1}$$

where $c_{\mathrm{i}d\sigma}$ ($c^{\dagger}_{\mathrm{i}d\sigma}$) annihilates (creates) electrons at the site $R_{\mathrm{i}}$ in the $d$-th layer ($d = 1, 2$) with spin $\sigma$ ($\sigma = \uparrow, \downarrow$) and $n_{\mathrm{i}d\sigma} =$

$c^{\dagger}_{id\sigma}c_{id\sigma}$. This system has intralayer nearest-neighbor hopping $t$ and interlayer next-nearest-neighbor hopping $t'$. These two layers have the same chemical potential $\mu$. We also consider the electron-electron Coulomb interaction $U$.

This chapter is organized as follows. In section 3.2 we calculate the dispersion relations and the DOS for the two types of bilayer triangular lattices at non-interacting limit ($U = 0$, refers to as the tight-binding model). The purpose is to study the special feature introduced by the two different structures: one with a finite gap, while the other is gapless, but both of them have two VHS, which affect their magnetic properties. In section 3.3, the spin susceptibility is studied by applying the random phase approximation(RPA) to estimate the critical value of Coulomb interaction $U_C$ at which the magnetic instability occurs. Then we obtain a rough estimation before non-perturbative approach is used to deal with electron-electron correlations. In section 3.4 we present numerical results obtained by the DQMC method.

For example, we study the ferromagnetic fluctuation of the system near one of the VHS in band filling region $1.6 \leq \langle n \rangle \leq 1.85$.

## 3.2 Tight-Binding Model on the Bilayer triangular Lattice

To gain some primary insights of the two structures, we begin with investigating their dispersions and DOS, then compare them with the single-layer case. At $U = 0$ the tight-binding model Hamiltonian can be diagonalized by using the Fourier transformation

$$\begin{aligned} c_{\mathbf{i}d\sigma} &= \frac{1}{\sqrt{N}} \sum_{\mathbf{k}} e^{i\mathbf{k}\cdot R_{\mathbf{i}}} c_{\mathbf{k}d\sigma} \\ c^{\dagger}_{\mathbf{i}d\sigma} &= \frac{1}{\sqrt{N}} \sum_{\mathbf{k}} e^{-i\mathbf{k}\cdot R_{\mathbf{i}}} c^{\dagger}_{\mathbf{k}d\sigma}. \end{aligned}$$

Then the Hamiltonian has a simple form of sum of $2 \times 2$ matrices

$$H = \sum_{\mathbf{k}\sigma} \begin{pmatrix} c^{\dagger}_{\mathbf{k}1\sigma} & c^{\dagger}_{\mathbf{k}2\sigma} \end{pmatrix} \begin{pmatrix} \alpha_{\mathbf{k}} & \beta_{\mathbf{k}} \\ \beta^{*}_{\mathbf{k}} & \alpha_{\mathbf{k}} \end{pmatrix} \begin{pmatrix} c_{\mathbf{k}1\sigma} \\ c_{\mathbf{k}2\sigma} \end{pmatrix}. \tag{3.2}$$

The elements of the $2 \times 2$ matrix are

$$\alpha_{\mathbf{k}} = -2t[\cos \mathbf{k} \cdot \vec{a_1} + \cos \mathbf{k} \cdot \vec{a_2} + \cos \mathbf{k} \cdot (\vec{a_1} - \vec{a_2})] - \mu$$

$$\beta_{\mathbf{k}} = -t'[1 + e^{i\mathbf{k}\cdot(\vec{a_1}-\vec{a_2})} + e^{-i\mathbf{k}\cdot\vec{a_2}}].$$

The $2 \times 2$ matrix can be diagonalized by the following linear transformation

$$c_{\mathbf{k}1\sigma} = \frac{\sqrt{2}}{2}\frac{|\beta_{\mathbf{k}}|}{\beta^*_{\mathbf{k}}}(d_{\mathbf{k}1\sigma} + d_{\mathbf{k}2\sigma}) \tag{3.3a}$$

$$c_{\mathbf{k}2\sigma} = \frac{\sqrt{2}}{2}(d_{\mathbf{k}1\sigma} - d_{\mathbf{k}2\sigma}), \tag{3.3b}$$

where we introduced another set of operators $d_{\mathbf{k}1\sigma}$ and $d_{\mathbf{k}2\sigma}$. Then the Hamiltonian has the diagonalized form as

$$H = \sum_{\mathbf{k}\sigma}(E^+ d^\dagger_{\mathbf{k}1\sigma} d_{\mathbf{k}1\sigma} + E^- d^\dagger_{\mathbf{k}2\sigma} d_{\mathbf{k}2\sigma}). \tag{3.4}$$

Because of double layers, the energy spectrum has two bands. For structure A,

$$E^\pm_{\mathbf{k}} = -tG(\mathbf{k}) - \mu \pm t'\sqrt{3 + G(\mathbf{k})}, \tag{3.5}$$

while for structure B,

$$E^\pm_{\mathbf{k}} = -tG(\mathbf{k}) - \mu \pm t'. \tag{3.6}$$

Here,

$$G(\mathbf{k}) = 2[\cos \mathbf{k} \cdot \overrightarrow{a_1} + \cos \mathbf{k} \cdot \overrightarrow{a_2} + \cos \mathbf{k} \cdot (\overrightarrow{a_1} - \overrightarrow{a_2})]. \qquad (3.7)$$

Fig. 3.2 represents the dispersion relations for the two structures along the symmetry path in the first Brillouin zone (BZ). Following the convention, $\mathbf{\Gamma}$ point is $(0, 0)$, $\mathbf{M}$ point is $(0, \pi)$ and $\mathbf{K}$ point is $(-\frac{2\pi}{3}, \frac{2\pi}{3})$. We calculate the dispersion relations for $t' = 0$ (the case of single layer), $t' = 0.4t$ and $t' = 0.8t$. The effects of $t'$ are evident: (1) for structure A, there is no gap between the two bands, while for structure B, there is an energy gap equal to $2t'$ at $\mathbf{K}$ point.

At finite temperatures, the electrons will occupy not only lower band but also upper band, so this energy gap will affect correlations between the two bands; (2) the bandwidth of spectrum becomes lager when $t'$ increases, so we expect that the Coulomb interaction will have smaller influences on the magnetic fluctuations. We also note that, as shown in Fig. 3.2,

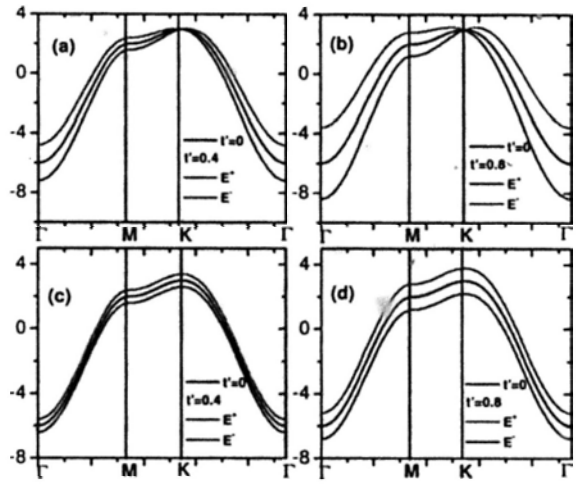


Figure 3.2: (Color online). Dispersion relations for structure A are represented in (a) and (b), while (c) and (d) represent structure B. The black curves represent single-layer triangular lattice $t' = 0$, the red curves represent the upper band $E^+$ and the blue curves represent the lower band $E^-$.

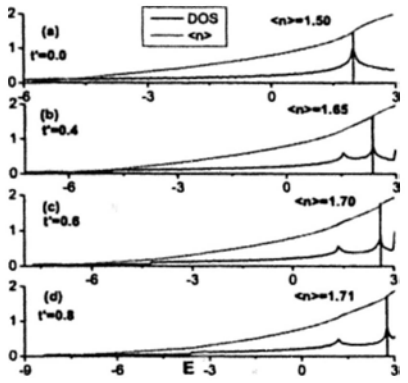


Figure 3.3: (Color online). DOS and band fillings of structure A are functions of energy: the red curves represent fillings $\langle n \rangle$ and the black lines represent the DOS computed from Eq. (3.5). The marked $\langle n \rangle$ are the filling values at one of the VHS.

there exist saddle points near **K** point, where the DOS has a large value.

In Fig. 3.3 and Fig. 3.4, in the single-layer triangular lattice case, $t' = 0$, there is only one VHS at filling $\langle n \rangle = 1.5$. When $t'$ is introduced the VHS becomes two separated peaks, and with $t'$ increasing, one peak moves toward the half filling while the other one toward the full filling. We will study the magnetic properties in the high band filling region. In particular, ferro-

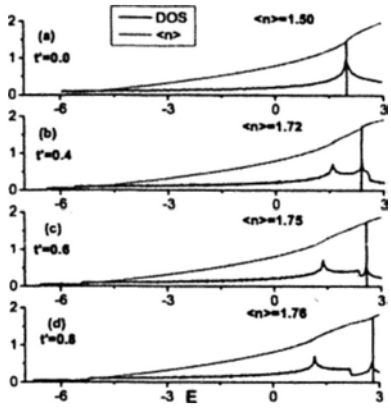


Figure 3.4: (Color online). DOS and band fillings of structure B are functions of energy: the red curves represent fillings $\langle n \rangle$ and the black lines represent the DOS computed from Eq. (3.6). The marked $\langle n \rangle$ are the filling values at one of the VHS.

magnetic fluctuations may arise due to this higher DOS near the Fermi level.

Comparing DOS of the two bilayer structures as shown in Fig. 3.3 and Fig. 3.4, in the high filling region, it is clear that DOS of structure A is larger than that of structure B, in particular their DOS at the VHS near the band top. In terms of Stoner's FM theory for itinerant electrons, ferromagnetic fluctuations tend to high DOS on the Fermi surface. So if we locate the Fermi

surface near VHS by adjusting chemical potential, we expect that the magnetic fluctuations are stronger in structure A than that in structure B. These expectations will be tested by the RPA calculations and QMC simulations which will be discussed in the following sections.

## 3.3 Spin Susceptibility for Tight-Binding Model

In this section, we calculate the spin susceptibility for the tight-binding model and then apply RPA to estimate critical values of Coulomb interaction when magnetic instabilities occur. The spin susceptibility in the $z$ direction at frequency $\omega = 0$ is given by

$$\chi_{dd'}(\mathbf{q}) = \frac{1}{N}\int_0^\beta d\tau \sum_{\mathbf{ij}} e^{i\mathbf{q}\cdot(R_\mathbf{i}-R_\mathbf{j})} \langle m_d^z(R_\mathbf{i},\tau) m_{d'}^z(R_\mathbf{j},0)\rangle \,, \quad (3.8)$$

where $m_d^z(R_\mathbf{i},0) = c_{d\mathbf{i}\uparrow}^\dagger c_{d\mathbf{i}\uparrow} - c_{d\mathbf{i}\downarrow}^\dagger c_{d\mathbf{i}\downarrow}$ and $m_d^z(R_\mathbf{i},\tau) = e^{H\tau} m_d^z(R_\mathbf{i},0) e^{-H\tau}$, and $N$ is the number of sites in one layer. The susceptibility has four components, $\chi_{11}$, $\chi_{12}$, $\chi_{21}$ and $\chi_{22}$.

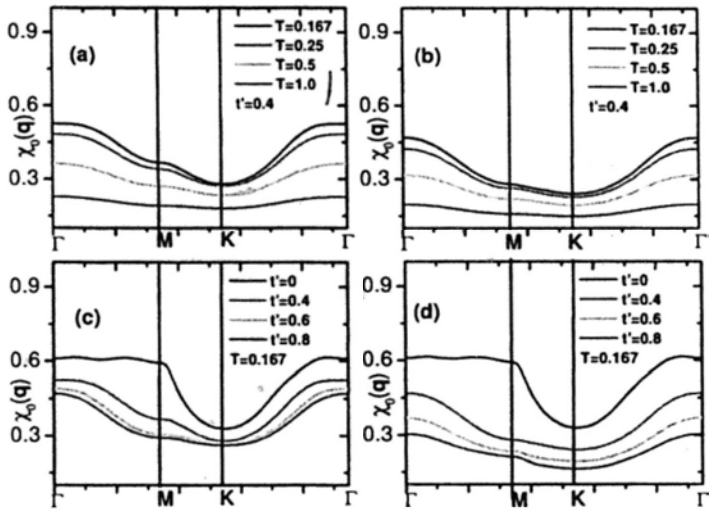


Figure 3.5: (Color online). (a) and (c) represent the results of structure A, and (b) and (d) represent the results of structure B. The momentum $\mathbf{q}$ is along $\mathbf{\Gamma} \longrightarrow \mathbf{M} \longrightarrow \mathbf{K} \longrightarrow \mathbf{\Gamma}$ in the first BZ.

Obviously, there exist the relations $\chi_{11} = \chi_{22}$ and $\chi_{12} = \chi_{21}^{*}$.

Because the Hamiltonian is solvable the spin susceptibility can be calculated analytically. After performing Fourier transformation, there are four terms in the spin susceptibility as the

followings:

$$\begin{aligned}
&\frac{1}{N}\int_0^\beta d\tau \sum_{\mathbf{ij}} e^{i\mathbf{q}\cdot(R_\mathbf{i}-R_\mathbf{j})} \left\langle c^\dagger_{\mathbf{i}d\sigma}(\tau)c_{\mathbf{i}d\sigma}(\tau)c^\dagger_{\mathbf{j}d'\sigma'}c_{\mathbf{j}d'\sigma'}\right\rangle \\
= &\frac{1}{N^3}\int_0^\beta d\tau \sum_{\mathbf{ij}}\sum_{\{\mathbf{k}\}} \left\langle c^\dagger_{\mathbf{k}_1 d\sigma}(\tau)c_{\mathbf{k}_2 d\sigma}(\tau)c^\dagger_{\mathbf{k}_3 d'\sigma'}c_{\mathbf{k}_4 d'\sigma'}\right\rangle \\
&\cdot e^{i\mathbf{q}\cdot(R_\mathbf{i}-R_\mathbf{j})+i(\mathbf{k}_1-\mathbf{k}_2)\cdot R_\mathbf{i}+i(\mathbf{k}_3-\mathbf{k}_4)\cdot R_\mathbf{j}}
\end{aligned} \tag{3.9}$$

where $c_{\mathbf{i}\sigma}(\tau) = e^{H\tau}c_{\mathbf{i}\sigma}e^{-H\tau}$. By the linear transformation of Eqs. (3.3a) and (3.3b), we calculate these correlation functions by applying Wick's theorem, and the details are presented in Appendix A. The intralayer spin susceptibility has the form as

$$\chi_{11}(\mathbf{q}) = B_1 + B_2 + B_3 + B_4, \tag{3.10}$$

and the four correlation functions are

$$B_1 = -\frac{1}{4N}\sum_{\mathbf{k},\sigma}\frac{\langle n_{\mathbf{k}+\mathbf{q}1\sigma}\rangle - \langle n_{\mathbf{k}1\sigma}\rangle}{E^+_{\mathbf{k}+\mathbf{q}} - E^+_\mathbf{k}}, \tag{3.11a}$$

$$B_2 = -\frac{1}{4N}\sum_{\mathbf{k},\sigma}\frac{\langle n_{\mathbf{k}+\mathbf{q}2\sigma}\rangle - \langle n_{\mathbf{k}1\sigma}\rangle}{E^-_{\mathbf{k}+\mathbf{q}} - E^+_\mathbf{k}}, \tag{3.11b}$$

$$B_3 = -\frac{1}{4N}\sum_{\mathbf{k},\sigma}\frac{\langle n_{\mathbf{k}+\mathbf{q}1\sigma}\rangle - \langle n_{\mathbf{k}2\sigma}\rangle}{E^+_{\mathbf{k}+\mathbf{q}} - E^-_\mathbf{k}}, \tag{3.11c}$$

$$B_4 = -\frac{1}{4N}\sum_{\mathbf{k},\sigma}\frac{\langle n_{\mathbf{k}+\mathbf{q}2\sigma}\rangle - \langle n_{\mathbf{k}2\sigma}\rangle}{E^-_{\mathbf{k}+\mathbf{q}} - E^-_\mathbf{k}}. \tag{3.11d}$$

The interlayer susceptibility also can be written as

$$\chi_{12}(\mathbf{q}) = C_1 + C_2 + C_3 + C_4, \tag{3.12}$$

there are also four terms as

$$C_1 = -\frac{1}{4N}\sum_{\mathbf{k},\sigma}\frac{\langle n_{\mathbf{k+q}1\sigma}\rangle - \langle n_{\mathbf{k}1\sigma}\rangle}{E^{+}_{\mathbf{k+q}} - E^{+}_{\mathbf{k}}}e^{i(\varphi_{\mathbf{k+q}}-\varphi_{\mathbf{k}})}, \tag{3.13a}$$

$$C_2 = \frac{1}{4N}\sum_{\mathbf{k},\sigma}\frac{\langle n_{\mathbf{k+q}2\sigma}\rangle - \langle n_{\mathbf{k}1\sigma}\rangle}{E^{-}_{\mathbf{k+q}} - E^{+}_{\mathbf{k}}}e^{i(\varphi_{\mathbf{k+q}}-\varphi_{\mathbf{k}})}, \tag{3.13b}$$

$$C_3 = \frac{1}{4N}\sum_{\mathbf{k},\sigma}\frac{\langle n_{\mathbf{k+q}1\sigma}\rangle - \langle n_{\mathbf{k}2\sigma}\rangle}{E^{+}_{\mathbf{k+q}} - E^{-}_{\mathbf{k}}}e^{i(\varphi_{\mathbf{k+q}}-\varphi_{\mathbf{k}})}, \tag{3.13c}$$

$$C_4 = -\frac{1}{4N}\sum_{\mathbf{k},\sigma}\frac{\langle n_{\mathbf{k+q}2\sigma}\rangle - \langle n_{\mathbf{k}2\sigma}\rangle}{E^{-}_{\mathbf{k+q}} - E^{-}_{\mathbf{k}}}e^{i(\varphi_{\mathbf{k+q}}-\varphi_{\mathbf{k}})}, \tag{3.13d}$$

here $\langle n_{\mathbf{k}1(2)}\rangle$ is the occupation number of electrons in band $E^{+(-)}$ with momentum $\mathbf{k}$, and the phase factor $e^{i\varphi_{\mathbf{k}}} = \frac{\beta_{\mathbf{k}}}{|\beta_{\mathbf{k}}|}$. For paramagnetic correlations, the mean value of occupation number obeys Fermi's distribution. Firstly, when $t' = 0$ the two bands are the same $E^{+}(\mathbf{k}) = E^{-}(\mathbf{k})$, and the Eq. (3.10) becomes

$$\chi_{11}(\mathbf{q}) = -\frac{1}{N}\sum_{\mathbf{k},\sigma}\frac{\langle n_{\mathbf{k+q}\sigma}\rangle - \langle n_{\mathbf{k}\sigma}\rangle}{E_{\mathbf{k+q}} - E_{\mathbf{k}}},$$

which is well known as the spin susceptibility in the single-band case while $\chi_{12}(\mathbf{q})$ becomes zero. Secondly, we compare these

Table 3.1: The critical value $U_C$ (unit of $t$) for structure A

| $U_C$ | $T =$ | 0.167 | 0.25 | 0.5 | 1.0 |
|---|---|---|---|---|---|
| $t' = 0$ | | 1.63 | 1.82 | 2.41 | 3.65 |
| $t' = 0.4$ | | 1.90 | 2.07 | 2.76 | 4.38 |
| $t' = 0.6$ | | 2.05 | 2.26 | 3.08 | 4.90 |
| $t' = 0.8$ | | 2.13 | 2.39 | 3.26 | 5.13 |

two correlation functions and observe that $\chi_{12}$ has an added phase factor and its four terms have different signs, which result in $\chi_{12}(\mathbf{q})$ being much smaller than $\chi_{11}(\mathbf{q})$. We expect that if the energy gap is larger, the correlation functions decrease and the spin susceptibilities become smaller accordingly. In view of the DOS, when the differences of energy $\Delta E = E_{\mathbf{k}+\mathbf{q}} - E_{\mathbf{k}}$ with given momentum $\mathbf{q}$ (either within one band or between two bands) varies more rapidly, correspondingly, the DOS will be smaller, as well as spin susceptibility.

Fig. 3.5 shows the total spin susceptibilities $\chi_0(\mathbf{q}) = \frac{1}{2}\sum_{dd'}\chi_{dd'}(\mathbf{q})$ of the tight-binding model at zero frequency for different $t'$. Cor-

Table 3.2: The critical value $U_C$ for structure B

| $U_C$ | $T =$ | 0.167 | 0.25 | 0.5 | 1.0 |
|---|---|---|---|---|---|
| $t' = 0$ | | 1.63 | 1.82 | 2.41 | 3.65 |
| $t' = 0.4$ | | 2.13 | 2.36 | 3.16 | 5.07 |
| $t' = 0.6$ | | 2.71 | 2.89 | 3.74 | 5.63 |
| $t' = 0.8$ | | 3.29 | 3.45 | 4.12 | 6.00 |

responding band fillings are marked in Fig. 3.3 and Fig. 3.4. In Fig. 3.5(a) and Fig. 3.5(b) the spin susceptibility will increase rapidly when the temperature is lowered, but at $T = 1.0t$, the curves of susceptibilities are very smooth. It is shown in Fig. 3.5(c) and Fig. 3.5(d) that spin susceptibilities become smaller as $t'$ increases. We compare the results of the two types of bilayer triangular lattices and find that the spin susceptibility of structure B is lower than that of structure A. It is because that when $t'$ increases, near the VHS the energy gap of structure B is magnified and the DOS decreases. In structure A the value of $\chi_0(\mathbf{K})$ is not sensitive to the change of $t'$ because the two energy

bands are degenerate at **K** point.

When interaction $U$ is turned on, the magnetic susceptibility within RPA is given by[66]

$$\chi(\mathbf{q}) = \frac{\chi_0(\mathbf{q})}{1 - U\chi_0(\mathbf{q})}. \tag{3.14}$$

Because we are interested in the region far away from the half filling, RPA predicts a transition between paramagnetic phase and FM phase with the high DOS when the critical condition is satisfied

$$1 - U\chi_0(\mathbf{q}) = 0. \tag{3.15}$$

At zero temperature, Eq. (3.15) becomes the Stoner criterion $U\rho(E_F) = 1$, where $\rho(E_F)$ is the DOS on the Fermi surface. On one hand when we tune band filling to localize the Fermi energy at the VHS, the system is unstable against ferromagnetic fluctuation. On the other hand Eq. (3.15) can be used to determine the critical strength $U_C$ as the transition appears.

In Tables 3.1 and 3.2, we present the results of $U_C$ with given

$t'$ and temperatures. Firstly, for the two structures with fixed value of $t'$, $U_C$ decreases as temperature is lowered. Secondly, when $t'$ is increasing, a larger $U_C$ is needed for the transition between paramagnetic and FM phases. Thirdly, with the same $t'$ and temperature, $U_C$ of structure A is a bit smaller than that of structure B. Moreover we expect that when parameters are the same for the two different systems, the ferromagnetic fluctuation is stronger in structure A than that in structure B. The results of RPA are reasonable because in Fig. 3.3 and Fig. 3.4, it is shown that for structure B the region between two singularities is wider and the DOS is lower than those for structure A.

Although the validity of RPA is limited, data presented in Table I and II are helpful to choosing appropriate parameters for QMC simulations. In the following section, we will observe that ferromagnetic fluctuations are noticeable both in structures A and B for certain parameters, but for some parameters the fluctuation in structure B is suppressed.

## 3.4 Spin Susceptibility for Hubbard Model

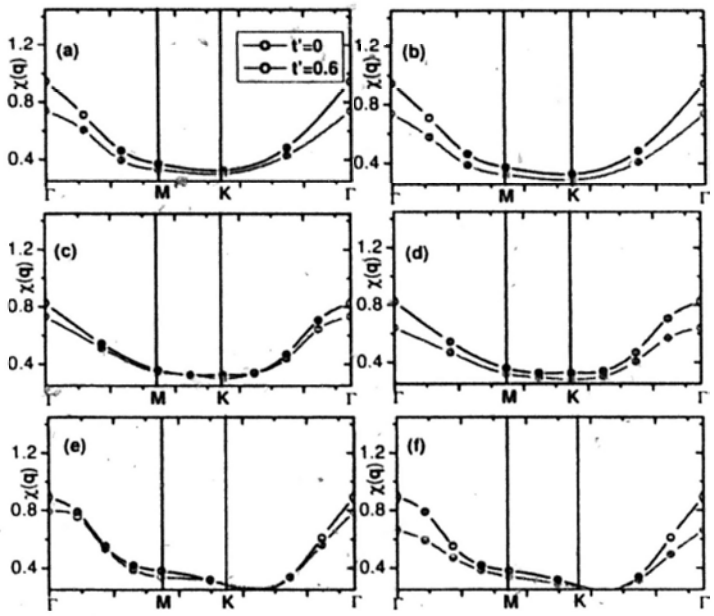


Figure 3.6: (Color online). The spin susceptibilities $\chi(\mathbf{q})$ in (a) and (b) are for the $36 \times 2$ lattice, in (c) and (d) are for the $48 \times 2$ lattice, in (e) and (f) are for the $64 \times 2$ lattice, with parameters $U = 8|t|$, $T = 0.33|t|$ and filling $\langle n \rangle = 1.7$. (a), (c) and (e) are for structure A and (b), (d) and (f) are for structure B. The momentum $\mathbf{q}$ is along $\Gamma \longrightarrow \mathbf{M} \longrightarrow \mathbf{K} \longrightarrow \Gamma$ in the first BZ.

To deal with electron-electron interaction non-perturbatively, we use the DQMC method[52] to simulate the single-band Hubbard model on the bilayer triangular lattices and treat this

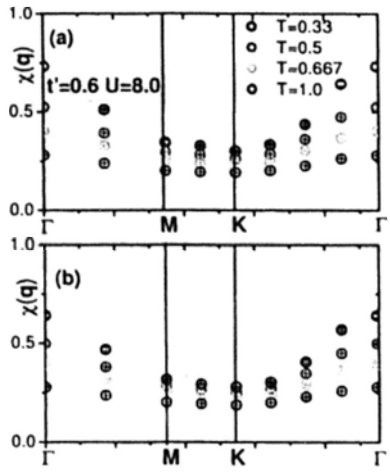


Figure 3.7: (Color online). The spin susceptibility $\chi(\mathbf{q})$ is represented versus temperature on the $48 \times 2$ lattice with $U = 8|t|$ and filling $\langle n \rangle = 1.7$. (a) is for structure A and (b) is for structure B.

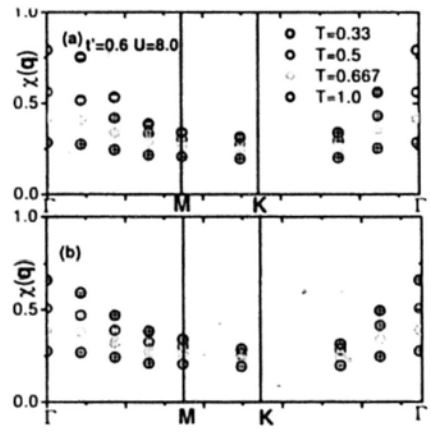


Figure 3.8: (Color online). The spin susceptibility $\chi(\mathbf{q})$ is represented versus temperature on the $64 \times 2$ lattice with $U = 8|t|$ and filling $\langle n \rangle = 1.7$. (a) is for structure A and (b) is for structure B.

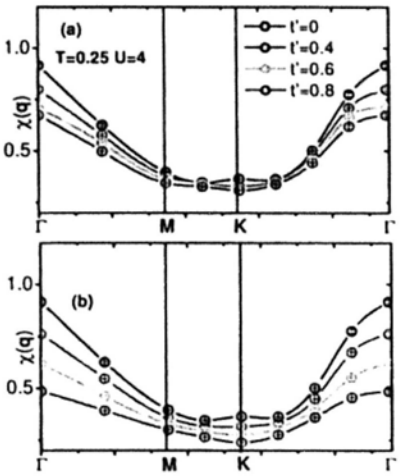


Figure 3.9: (Color online). The spin susceptibility $\chi(\mathbf{q})$ is represented versus $t'$ on the $48 \times 2$ lattice with filling $\langle n \rangle = 1.7$, $U = 4|t|$ and $T = 0.25|t|$. (a) is for structure A and (b) is for structure B.

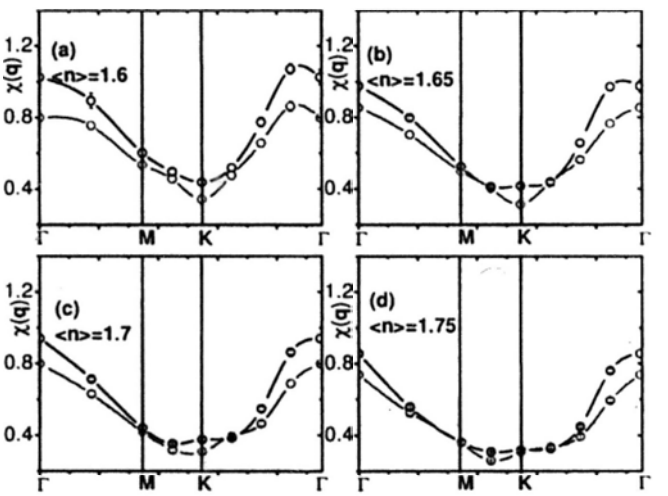


Figure 3.10: (Color online). The spin susceptibility $\chi(\mathbf{q})$ is represented versus filling on the $48 \times 2$ lattice for $U = 4|t|$, $T = 0.167|t|$ and $t' = 0.4t$. The black curves are for structure A and the red curves are for structure B.

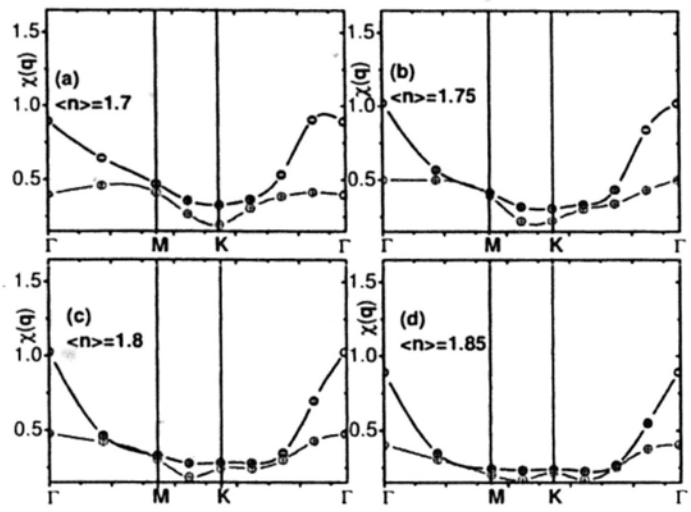


Figure 3.11: (Color online). The spin susceptibility $\chi(\mathbf{q})$ is represented versus filling on the $48 \times 2$ lattice for $U = 4|t|$, $T = 0.167|t|$ and $t' = 0.8t$. The black curves are for structure A and the red curves are for structure B.

system as a grand canonical ensemble at finite temperatures. We mainly calculate the spin susceptibility by the unequal-time Green's function in the imaginary-time direction. We perform DQMC simulation on this model for three sizes of lattice, $36 \times 2$, $48 \times 2$, and $64 \times 2$ sites. Simulations were done for both two structures as shown in Fig. 3.1. In the filling regions under investigation, the behaviors of the spin susceptibilities are qualitatively similar. We present here the results at band filling $\langle n \rangle = 1.7$.

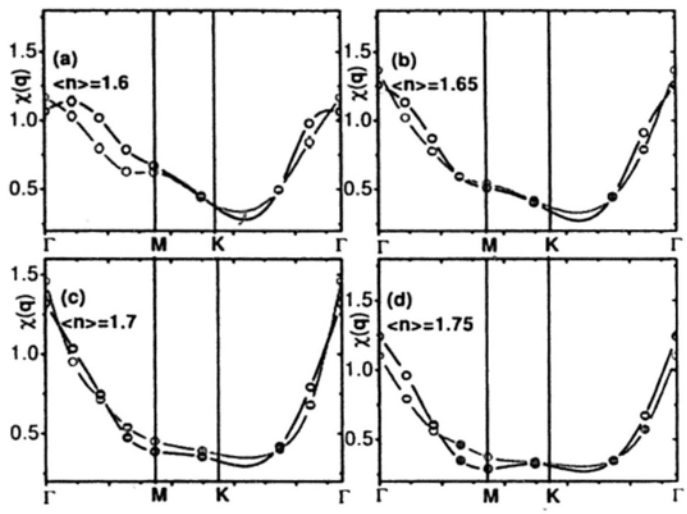


Figure 3.12: (Color online). The spin susceptibility $\chi(\mathbf{q})$ is represented versus filling on the $64 \times 2$ lattice for $U = 4|t|$, $T = 0.167|t|$ and $t' = 0.4t$. The black curves are for structure A and the red curves are for structure B.

Fig. 3.6 shows $\chi(\mathbf{q})$ versus momentum $\mathbf{q}$ along the symmetry path in the first BZ for $U = 8|t|$ and $T = 0.33|t|$. The critical values of Coulomb interaction, $U_C$, based on RPA results(with the same parameters $t'$ and $T$) in Sec. 3.3, are much smaller than the value we adopt here ($U = 8|t|$). So magnetic fluctuations in the three structures, the single-layer triangular lattices($t' = 0$) and the two types of bilayer lattices with ($t' = 0.6t$), are evident, and in the six sub-pictures we compare their spin susceptibili-

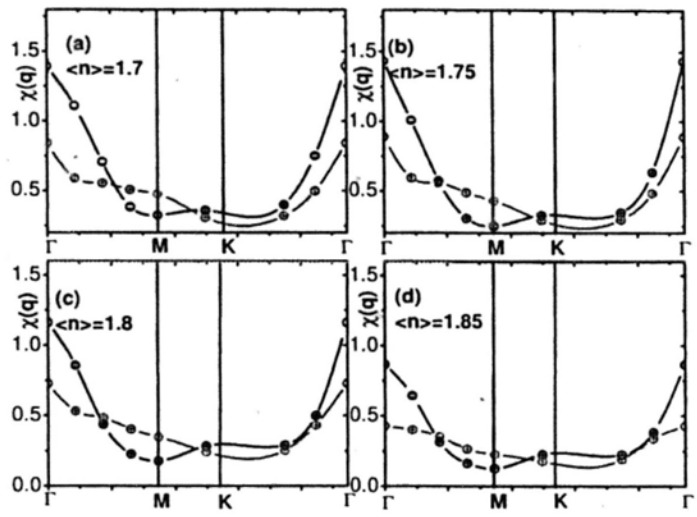


Figure 3.13: (Color online). The spin susceptibility $\chi(\mathbf{q})$ is represented versus filling on the $64 \times 2$ lattice for $U = 4|t|$, $T = 0.167|t|$ and $t' = 0.8t$. The black curves are for structure A and the red curves are for structure B.

ties. In both $t' = 0$ and $t' = 0.6t$ cases, $\chi(\mathbf{q})$ have broad peaks around the $\mathbf{\Gamma}$ points, indicating obvious ferromagnetic fluctuations in these systems. Compared to the spin susceptibilities in Fig. 3.5 it is seen that considerable Coulomb interaction greatly intensifies magnetic fluctuations. Moreover when $t'$ increases, $\chi(\mathbf{0})$ ($\mathbf{\Gamma}$ point) decreases and the ferromagnetic fluctuations are suppressed. On the coupled bilayer square lattices, the similar results for the anti-ferromagnetic fluctuations were reported

[16]. We may attribute this phenomenon to the Stoner's theory that the ferromagnetic fluctuations tend to the high DOS on the Fermi surface. When $t'$ is introduced the original singularity is divided into two peaks, as a result, the DOS near these two peaks is lowered.

In Fig. 3.7 and Fig. 3.8, we present the spin susceptibilities on the $48 \times 2$ and $64 \times 2$ lattice, respectively. We fix band filling $\langle n \rangle = 1.7$ and $U = 8|t|$, which is about the bandwidth. At temperature $T = 0.33|t|$, it is clear that there are ferromagnetic fluctuations, but at higher temperature $T = 1.0|t|$, the curves of $\chi(\mathbf{q})$ become much smooth, namely, the ferromagnetic fluctuations are not noticeable.

In Fig. 3.9, we study the spin susceptibilities $\chi(\mathbf{q})$ versus $t'$ with $U = 4|t|$ and temperature $T = 0.25|t|$. The band filling $\langle n \rangle$ is fixed at 1.7 with high DOS, as is shown in Fig. 3.3 and Fig. 3.4. We do the calculations on the $48 \times 2$ lattice. To emphasize the effects of $t'$, we also show the results of the single-

layer triangular lattices in every sub-figure. Fig. 3.9(a) shows the results of structure A and Fig. 3.9(b) shows the results of structure B. The rise in $\chi(\mathbf{q})$ with $t'$ decreasing can be seen to occur in both two types of bilayer structures. It is interesting that the values of $\chi(\mathbf{0})$ in structure B decrease more rapidly than that in structure A with $t'$ increasing. Between $\mathbf{M}$ and $\mathbf{K}$ points in the first BZ of structure A, the spin susceptibility curves with different $t'$ are close to each other. It is because that the two energy bands are degenerate at the $\mathbf{K}$ point. On the contrary, the structure B with energy gap at this point does not have the same behavior.

With extensive DQMC simulation data, let us compare magnetic properties of the two types of bilayer triangular lattices in detail with Figs. 3.10-3.13. We observe that the VHS for two structures with $t' = 0.4t$ are localized in the filling regions between 1.6 and 1.75. With $t' = 0.8t$ the VHS are in the zones from 1.7 to 1.85. When $t' = 0.4t$ the spin susceptibility of structure

B is little lower than that of structure A on the 48 × 2 lattice, but this difference is not evident on the 64 × 2 lattice. When $t'$ increases to $0.8t$, the ferromagnetic fluctuations in structure B decay monotonically but in structure A ferromagnetic fluctuations are still obvious. We take $U = 4|t|$, $T = 0.167|t|$ and $t' = 0.4t,\ 0.8t$. Given the results of RPA in Tables 3.1 and 3.2, when $t' = 0.4t$ the critical values $U_C$ of the two structures are about 2—t—, one half of the value ($U = 4|t|$) we used in simulations. However when $t' = 0.8t$, the critical value $U_C$ of structure A is still about $2|t|$ but for structure B, $U_C$ approaches to $4|t|$. In this case, the strength of electron-electron interaction is enough to induce ferromagnetic fluctuations in structure A but not in structure B.

Figs. 3.10-3.13 show band filling dependence of $\chi(\mathbf{q})$. For $t' = 0.4t$ and $\langle n \rangle = 1.6$ the peak of $\chi(\mathbf{q})$ near the $\mathbf{\Gamma}$ point is broadened, and when the band filling varies from 1.65 to 1.7 the peak of $\chi(\mathbf{q})$ at $\mathbf{\Gamma}$ point is strengthened, as band filling reaches

1.75 the value of $\chi(\mathbf{0})$ begins to decrease. These phenomena exist in both structures A and B. When $t' = 0.8t$ and band filling varies from 1.75 to 1.85 there are very weak ferromagnetic fluctuations in structure B. In contrast, there are distinct ferromagnetic fluctuations in structure A, which become the strongest when filling reaches 1.75.

We have studied the magnetic properties of two types of bilayer triangular lattices. We calculated the energy spectrum and the DOS based on the tight-binding model. When the interlayer hopping $t'$ is introduced, the spectrum has two bands. The energy bands of structure A are degenerate at $\mathbf{K}$ point. On the contrary, for structure B, there is a considerable gap between the two bands. Compared to the case of single layer, the DOS of bilayer structure is lower in the filling region $\langle n \rangle = 1.5 - 1.9$. Moreover, there are two singularities in the DOS for the bilayer triangular lattices. By performing the RPA calculations, we obtained the critical values of the Coulomb interaction $U_C$ of the

magnetic instability. The results showed that with increasing $t'$, larger $U_C$ is needed. For the same $t'$, structure B requires a larger $U_C$ than that of structure A.

We have carried out a DQMC simulation for the single-band Hubbard model on the bilayer triangular lattices. By calculating the spin susceptibility, we studied the magnetic properties of the bilayer systems near the VHS. By the itinerant electron magnetism theory, the ferromagnetic fluctuations tend to the high DOS on the Fermi surface. Compared to the single-layer triangular lattice case, when $t'$ is gradually increasing, ferromagnetic fluctuations are suppressed in both structures A and B.

We have explained the effects of $t'$ on the FM fluctuations in terms of the DOS. After analyzing the spin susceptibilities with the same $t'$, the conclusion is that the FM fluctuations are weaker in structure B than those in structure A. This helps us in understanding the effects of frustration on the magnetic properties of various structures.

---

□ **End of chapter.**

# Chapter 4

# Ferromagnetism in Graphene

## 4.1 Introduction

This chapter addresses the issue of FM in graphene-based samples. To study this kind of magnetic correlations in graphene, we systematically carry out QMC simulations of the Hubbard model on a honeycomb lattice. In the filling region below the VHS, the system shows a short-range ferromagnetic correlation, which is slightly strengthened by the on-site Coulomb interaction and markedly by the next-nearest-neighbor hopping integral, with an estimated Weiss temperature about 580K. The

ferromagnetic properties depend on the electron filling strongly, which may be manipulated by the electric gate. Due to its resultant high controllability of FM, graphene-based samples may facilitate the new development of many applications. In section 4.2, we present a brief introduction of lattice structure and electronic properties of graphene in the framework of tight-binding model. We mainly focus on the DOS of graphene when introducing the next-nearest-neighbor hopping. In section 4.3, we do the DQMC simulation to calculate the spin susceptibility of graphene and we find the room-temperature FM in this system. In section 4.3, we propose a scheme of controllability of Ferromagnetism in graphene through two physical quantities, one is electron filling, the other one is next-nearest-neighbor hopping integrals.

## 4.2 Electronic Properties of Graphene in Tight-Binding Model

The structure of graphene can be described in terms of two interpenetrating triangular sublattices, A and B, and its low energy electric and magnetic properties can be well described by the Hubbard model on a honeycomb lattice[47, 48, 49, 50, 51],

$$\begin{aligned} H &= -t\sum_{i\eta\sigma} a^{\dagger}_{i\sigma} b_{i+\eta\sigma} + t'\sum_{i\gamma\sigma}(a^{\dagger}_{i\sigma} a_{i+\gamma\sigma} + b^{\dagger}_{i\sigma} b_{i+\gamma\sigma}) + \text{h.c.} \\ &+ U\sum_{i}(n_{ai\uparrow} n_{ai\downarrow} + n_{bi\uparrow} n_{bi\downarrow}) + \mu\sum_{i\sigma}(n_{ai\sigma} + n_{bi\sigma}) \end{aligned} \quad (4.1)$$

where $t$ and $t'$ are the nearest and next-nearest-neighbor hopping integrals respectively, $\mu$ is the chemical potential, and $U$ is the Hubbard interaction. Here, $a_{i\sigma}$ ($a^{\dagger}_{i\sigma}$) annihilates (creates) electrons at site $\mathbf{R}_i$ with spin $\sigma$ ($\sigma$=$\uparrow,\downarrow$) on sublattice A, $b_{i\sigma}$ ($b^{\dagger}_{i\sigma}$) annihilates (creates) electrons at the site $\mathbf{R}_i$ with spin $\sigma$ ($\sigma$=$\uparrow,\downarrow$) on sublattice B, $n_{ai\sigma}$=$a^{\dagger}_{i\sigma} a_{i\sigma}$ and $n_{bi\sigma}$=$b^{\dagger}_{i\sigma} b_{i\sigma}$.

Our main numerical calculations were performed on a double-48 sites lattice, as sketched in Fig. 1, where blue circles and

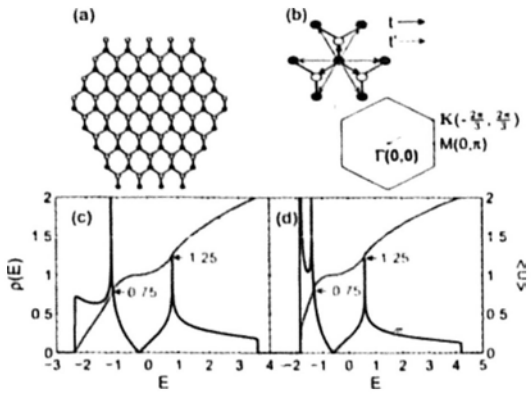


Figure 4.1: (Color online) (a) Sketch of graphene with double-48 sites; (b) First BZ and the high symmetry direction (red line); (c) DOS (dark lines ) and fillings $\langle n \rangle$ (red lines ) as functions of energy with $t'$=0.10t; and (d) $t'$=0.20t.

yellow circles indicates A and B sublattices, respectively. The energy bands of model tight-binding model of Eq. (4.1) are

$$E_{\pm}(\mathbf{k}) = \pm t\sqrt{3+f_{\mathbf{k}}} + t' f_{\mathbf{k}}, \tag{4.2}$$

$$f_{\mathbf{k}} = 2\cos(\sqrt{3}k_y a) + 4\cos(\frac{\sqrt{3}}{2}k_y a)\cos(\frac{3}{2}k_x a)$$

where the plus sign applies to the upper ($\pi$) and the minus sign to the lower ($\pi^*$) band, and the bandwidth is $W$=6$|t|$. It is clear from Eq. (4.2) that the spectrum is symmetric around zero if $t'$=0. For finite values of $t'$ the electron-hole symmetry is broken

and both $\pi$ and $\pi^*$ bands become asymmetric. The structure of the honeycomb lattice leads to the well known massless-Dirac-fermion-like low energy excitations and the two VHS in the DOS (marked in Fig. 1) at $<n>$=0.75 and 1.25 corresponding to $E$=$-2t' \pm t$, respectively as $t' < t/6$. While when $t' \geq t/6$, a third VHS appears at the lower band edge, which is a square root singularity marking the flattening of the energy band near $\Gamma$ point. They determine much of system's properties.

In graphene, the value of $t$ reported in the literature[51] ranges from 2.5 to 2.8 eV, while the value of $U$ can be taken from the estimation in polyacetylene[51, 67, 68, 69, 70], ($U \simeq 6.0 - 16.93$ eV). Thus, we expect the ratio $U/|t|$ to be $2.2 \sim 6.0$, which is around the range of half-bandwidth to bandwidth, where the mean filed theory does not work well while the DQMC simulation is a useful tool [59]. Moreover, we notice that earlier studies on graphene assumed that $t'$=0. This assumption, however, is not warranted since there is overlap between carbon $\pi$

orbits in the same sublattice. The exact value of $t'$ is not known but an *ab initio* calculation [71] found that $t'/t$ ranges from 0.02 to 0.2 depending on the tight-binding parameterizations. Therefore, it is necessary to study the ferromagnetic fluctuations within the Hubbard model on the honeycomb lattice by including $t'$.

## 4.3 Ferromagnetic Correlation in Graphene

In the followings, we show that the behaviors of magnetic correlation are qualitatively different in two filling regions separated by the VHS at $<n>$=0.75. In the filling region below the VHS point, the system shows a short-ranged ferromagnetic correlation and the on-site Coulomb interaction tends to strengthen ferromagnetic fluctuation. The ferromagnetic properties depend on the electron filling, which may be manipulated by the electric gate. Furthermore, the ferromagnetic fluctuation is strengthened markedly as $t'$ increases. Our results highlight the cru-

cial importance of electron filling and the next-nearest-neighbor hopping in graphene. The resultant high controllability of FM may facilitate the new development of spintronics and quantum modulation.

To study ferromagnetic fluctuations, we define the spin susceptibility in the $z$ direction at zero frequency,

$$\chi(q) = \int_0^\beta d\tau \sum_{d,d'=a,b} \sum_{i,j} e^{iq\cdot(i_d - j_{d'})} \langle \mathrm{m}_{i_d}(\tau) \cdot \mathrm{m}_{j_{d'}}(0) \rangle \qquad (4.3)$$

where $m_{i_a}(\tau)=e^{H\tau} m_{i_a}(0) e^{-H\tau}$ with $m_{i_a}=a^\dagger_{i\uparrow}a_{i\uparrow}-a^\dagger_{i\downarrow}a_{i\downarrow}$ and $m_{i_b}=b^\dagger_{i\uparrow}b_{i\uparrow}-b^\dagger_{i\downarrow}b_{i\downarrow}$. We measure $\chi$ in unit of $|t|^{-1}$. Here, $\chi(\Gamma)$ measures ferromagnetic correlation while $\chi(K)$ measures anti-ferromagnetic correlation. In the DQMC method, a breakup of the discretized imaginary-time evolution operator introduces a systematic error proportional to $(\Delta\tau)^2 U$ (with $\Delta\tau$ describes the imaginary time). We have used $\Delta\tau$ =0.125, which guarantees $(\Delta\tau)^2 U < 0.125$ for $U$ <8|t|, leading to negligible systematic error (within a few percent). In our simulations, 8000 sweeps were used to equilibrate

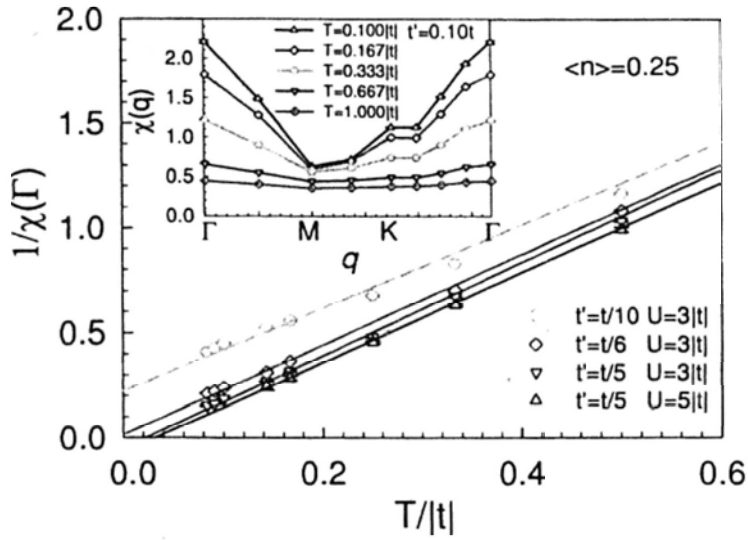


Figure 4.2: (Color online) At $<n>$=0.25, inverse of magnetic susceptibility, $1/\chi(q{=}\Gamma)$ versus temperature with $U$=3|t|, $t'$=$t/10$, $t/6$, and $t/5$. Fitted line $1/\chi(\Gamma){=}\alpha(T-\Theta)$ are also shown. Inset: Magnetic susceptibility $\chi(q)$ versus $q$ at different temperatures with $t'$=$0.10t$ and $U$=$3|t|$.

the system. An additional 30000 sweeps were then made, each of which generated a measurement. These measurements were split into ten bins which provide the basis of coarse-grain averages and errors estimates based on standard deviations from the average.

We first present temperature dependence of the magnetic correlations at $<n>$=0.25 with different $t'$ and $U$. Fig. 4.2 shows

$1/\chi(q{=}\Gamma)$ versus temperature at $U{=}3|t|$ and for $t'{=}t/10$, $t/6$, and $t/5$. Data for $U{=}5|t|$ as $t'{=}t/5$ are also shown. The reason for choosing $<n>{=}0.25$ will be clear when we discuss filling dependance later (e.g., Fig. 5). In the inset, we present $\chi(q)$ versus momentum $q$ at different temperatures with $t'{=}t/10$ for $U{=}3|\mathrm{t}|$. It is obvious that $\chi(q)$ has strong temperature dependence and one observes that $\chi(M)$ and $\chi(K)$ grow much slower than $\chi(\Gamma)$ with decreasing temperatures. Moreover, $1/\chi(\Gamma)$ exhibits Curie-like behavior as temperature decreases from $|t|$ to about $0.1|t|$. Fitting the data as $1/\chi(\Gamma){=}\alpha(T-\Theta)$ (solid lines in Fig.4.2) shows that Weiss temperature, $\Theta$ is about $0.02|\mathrm{t}|{\simeq}\ 580K$ at $t'{=}t/5$, and we also note that both $\Theta$ and $\chi(\Gamma)$ is enhanced slightly as the on-site Coulomb interaction is increased. Positive values of $\Theta$ indicate that the curves of $1/\chi(\Gamma)$ start to bend at some low temperatures and probably converge to zero as $T \rightarrow 0$, *i.e.*, $\chi(\Gamma)$ diverges. This demonstrates the existence of ferromagnetic state in graphene.

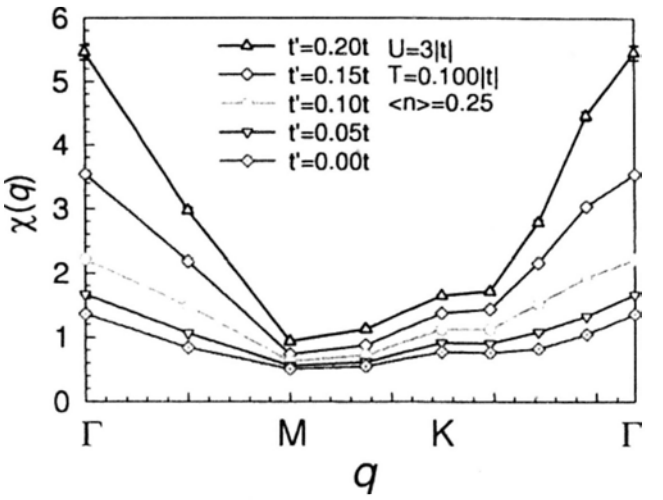


Figure 4.3: (Color online) Magnetic susceptibility $\chi(q)$ versus momentum $q$ at different $t'$, here $U$=3 |t|, <$n$>=0.25 and $T$=0.10|t|.

From Fig. 4.2, we may also notice that $t'$ plays a remarkable effect on the behavior of $\chi(q)$, and results for $\chi(q)$ dependent on $q$ with different $t'$ at $U$=3$|t|$, $T$=0.10$|t|$ and <$n$>=0.25 have been shown in Fig. 4.3. Clearly, $\chi(\Gamma)$ gets enhanced greatly as $t'$ increases, while $\chi(M)$ and $\chi(K)$ increase only slightly. Thus, again it is significant to demonstrate that ferromagnetic fluctuation gets enhanced markedly as $t'$ increases. Furthermore, the strong dependance of FM on $t'$ suggests high controllability of FM in graphene by tuning $t'$[72, 73, 74].

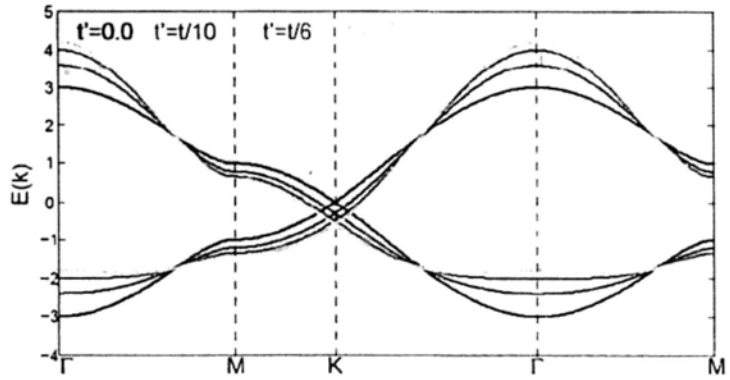


Figure 4.4: (Color online) Band structure of graphene in terms of Eq. 4.2. The curves, in the first BZ and along the symmetry path $\mathbf{\Gamma} \longrightarrow \mathbf{M} \longrightarrow \mathbf{K} \longrightarrow \mathbf{\Gamma} \longrightarrow \mathbf{M}$ is for $t' = 0$, $t' = t/10$, $t' = t/6$, and $t' = t/5$.

Here we focus on possible ferromagnetic solutions in our system. Remembering the singularity in the DOS shown in Fig. 4.1, one obtains a strongly asymmetric DOS showing a square-root singularity at the lower band edge as $t' \geq t/6$, which marks the flattening of the energy band near $\Gamma$ point. In Fig. 4.4, we present the band structure of graphene in terms of Eq. 4.2 and we can see the lower band near $\Gamma$ point becomes flatter as $t'$ increasing. The situation present in our system is very similar to the 'flat band' scenario. The flat band FM was introduced

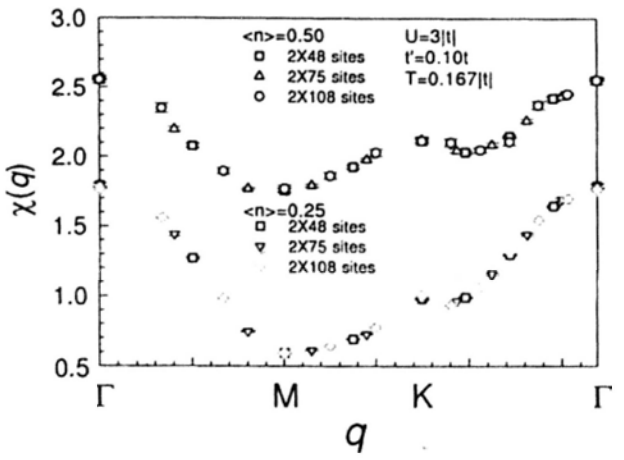


Figure 4.5: (Color online) Magnetic susceptibility $\chi(q)$ versus momentum $q$ on different lattices with $U$=3|t|, $T$=0.167|t| and $t'$=0.10$t$. Data at $<n>$=0.50 and 0.25 are plotted.

by Mielke and Tasaki[75, 76], and they proved the existence of FM under conditions where the ferromagnetic ground state appears due to a dispersionless (flat) lowest lying band. This flat band introduces a huge degeneracy of the ground state at $U$=0, which is lifted by the Coulomb interaction. Former studies for an asymmetric DOS already showed the existence of FM in such a situation[77, 78]. Consequently, we have to expect FM in our system, too.

We next present $\chi(q)$ versus momentum $q$ in Fig. 4.5 for $t'$=0.1$t$, $T$=0.167$|t|$, and $U$=3$|t|$ on three set of lattices, double-48, double-75 and double-108 sites at electron filling $<n>$=0.50 and 0.25, respectively. A broad peak around $\Gamma$ point in the first BZ once again indicates the existence of ferromagnetic fluctuation. We also note that data from different lattices agree with each other within statistical error. Since $\chi(q)$ obtained by summing up all lattice sites does not increase with lattice size, we conclude that ferromagnetic correlations are short ranged at $t'$=0.1$t$. Furthermore, Fig. 4.5 shows that $\chi(q)$ is sensitive to electron filling, and it is strengthened when electron fillings moves to the region where the VHS locates, namely, from $<n>$=0.25 to $<n>$=0.50.

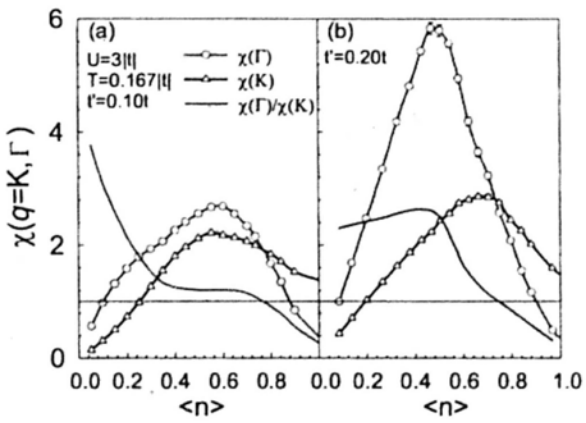


Figure 4.6: (Color online) Magnetic susceptibility $\chi(q{=}\Gamma)$ (red) and $\chi(q{=}K)$ (dark) versus electron filling at $U{=}3|t|$ and $T{=}0.167|t|$ with (a) $t'{=}0.1t$ and (b) $t'{=}0.2t$.

## 4.4 Controllability of Ferromagnetic Correlation in Graphene

A great deal of current activity in graphene arises from its technological significance as a novel semiconductor material where carrier density can be controlled by an external gate voltage[21, 33]. To understand filling dependence of magnetic correlations intuitively, we present $\chi(\Gamma)$ (red), $\chi(K)$ (dark), and their ratio $\chi(\Gamma)/\chi(K)$ (blue) versus filling for (a) $t'$=0.1$t$ and (b) $t'$=0.2$t$ in Fig. 4.6, with $U$=3$|t|$ and $T$=0.167$|t|$. There is a crossover between $\chi(\Gamma)$ and $\chi(K)$, which indicates that the behaviors of $\chi(q)$ are qualitatively different in two filling regions separated by the VHS at $<n>$=0.75, where the ratio is 1. This is due to the competition between ferromagnetic and antiferromagnetic fluctuations. The antiferromagnetic correlations are strong around the hall-filing case, and they may dominate the shape of $\chi(q)$ in a wide filling range up to the VHS. The effect of $t'$ in enhanc-

ing ferromagnetic fluctuation also can be seen by comparing Figs. 4.6(a) with (b). At electron filling $<n>$=0.25, the ratio of $\chi(\Gamma)/\chi(K)$ is about maximum for $t'$=0.2$t$ and is substantial for $t'$=0.1$t$, which is the reason why did we choose electron filling 0.25 in Figs. 4.2-4.5.

Finally, we discuss the possible practical setup for high controllability of FM in graphene-based samples on the basis of our analysis. From Fig. 4.5, especially the global picture shown in Fig. 4.6, it is clear that the strength of ferromagnetic correlation strongly depends on the electron filling, which may be manipulated by the electric gates in graphene, since $n \propto V_g$[21, 33, 34]. The filling region for inducing FM required here likely exceeds the current experimental ability. In fact, the challenge of increasing the carrier concentration in graphene is indeed very important and it is a topic now in progress. The second gate (from the top) and/or chemical doping methods are devoted to achieving higher carrier density[79, 80, 81], and

recently, G. Li, *et. al* have induced VHS within the range of Fermi energy achievable by gate tuning, which opens intriguing prospects for VHS engineering of electronic phases in graphene-based materials[82]. Moreover, the hydrogenated nanographite is predicated to show spontaneous magnetism[83], ferromagnetic insulators deposited on graphene can induce ferromagnetic correlation in graphene[84] and the room-temperature FM coming from the defects on graphene has been observed[85]. Hence, our results present here indicate the electron filling markedly affects the magnetic properties of graphene, and the high controllability of FM may be realized in ferromagnetic graphene-based samples. Furthermore, the change of ferromagnetic correlation with $t'$ may also lead to high controllability of FM in graphene. For example, one can tune $t'$ by varying the spacing between lattice sites. Tuning $t'$ can also be realized in a triangular optical bilayer lattice of dipolar atoms[72, 73, 74].

In summary, we have presented exact numerical results on

the magnetic correlation in the Hubbard model on a honeycomb lattice. At temperatures where the DQMC were performed, we found ferromagnetic fluctuation dominates in the low electron filling region, and it is slightly strengthened as interaction $U$ increases. The ferromagnetic correlation showed strong dependance on the electron filling and the next-nearest-neighbor hoping integral. This provides a route to manipulate FM in ferromagnetic graphene-based samples by the electric gate or varying lattice parameters. The resultant high controllability of FM in ferromagnetic graphene-based samples may facilitate the new development of many applications.

□ **End of chapter.**

# Chapter 5

# Magnetic Impurity in Graphene

## 5.1 Introduction

In this chapter, we theoretically examine a localized impurity atom on the graphene sheet. We use non-perturbative numerical method, DQMC based on HF algorithm [65], to study the local moments on impurity hybridizing with inner shell electrons in graphene. In section 5.2, we present the Anderson Hamiltonian in graphene describing an adatom, with Coulomb interactions between unaligned spins, hybridizing with carbon atoms in graphene. And then we give a brief introduction of Kondo

problem in this system which is very sensitive to the DOS on the Fermi surface. In section 5.3, we focus on the chemical potential of graphene which can be used to tune the Fermi energy experimentally. Through calculating the local moments and spin susceptibility of impurity we find that it is possible to switch on and off the local moments of impurity with medium or large hybridizations by tuning chemical potential of graphene. In section 5.4, we use maximum entropy method to study the spectral density of impurity which can be measured by the experiments of scanning tunneling microscope. We mainly find two unconventional behaviors distinguishing from those of impurity in normal metal.

## 5.2 Anderson Impurity Model in Graphene and Kondo Problem

Our starting point is Anderson impurity model describing an impurity with a single orbital of energy $\varepsilon_d$ and Coulomb repulsion $U$. In graphene,the impurity couples with the conduction electron states of carbon atom with hybridization $V$. The total Hamiltonian is $H = H_0 + H_1 + H_2$, and the first term is tight-binding Hamiltonian of graphene

$$H_0 = -t \sum_{<ij>,\sigma} [a^\dagger_{i\sigma} b_{j\sigma} + \text{H.c.}] - \mu \sum_{i\sigma} [a^\dagger_{i\sigma} a_{i\sigma} + b^\dagger_{i\sigma} b_{i\sigma}], \quad (5.1)$$

where $a^\dagger_i$ and $b^\dagger_i$ create electrons with spin $\sigma$ at sites $\mathbf{R}_{ia}$ and $\mathbf{R}_{ib}$ on sublattices $A$ and $B$, respectively. The hopping energy $t$ is about 2.8 eV [51] and $\mu$ is chemical potential which can be tuned by gate voltage. There are two bands, the $\pi$ and $\pi^*$ bands, with width of $3t$ touch each other at six Dirac points in

the first Brillouin zone. The second term is impurity part as

$$H_1 = \sum_\sigma \varepsilon_d d_\sigma^\dagger d_\sigma + U d_\uparrow^\dagger d_\uparrow d_\downarrow^\dagger d_\downarrow . \tag{5.2}$$

Here $d_\sigma^\dagger$ creates an electron with spin $\sigma$ at impurity orbital. The last term of Hamiltonian $H_2$ is the hybridization between impurity and graphene atom as

$$H_2 = V \sum_\sigma [a_{0\sigma}^\dagger d_\sigma + \text{H.c.}] , \tag{5.3}$$

here we consider the impurity is located on the top of the site $\mathbf{R}_{0a}$ of sublattice $A$ seen in Fig. 5.1, however if we apply Fourier transformation to $H_2$ it is clear that impurity is hybridized with all conduction electron states in momentum space.

The Fermi energy is one of the most interesting physical quantity experimentally which can be tuned by gate voltage [38]. On one hand, in the terms of Anderson's discussion[86] when $\varepsilon_d < E_F < \varepsilon_d + U$ the impurity site is singly occupied and has a local moment. So through changing the Fermi energy, we can control the local moment of impurity itself. On the other

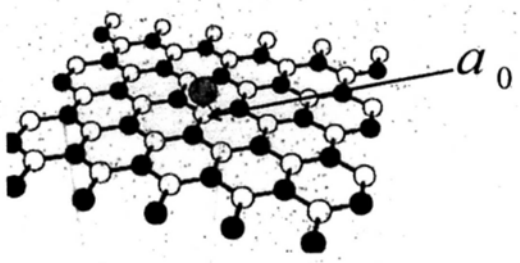


Figure 5.1: (Color online).The impurity atom represented by the red circle is on the open surface of graphene sheet and hybridizes with carbon atom at $a_0$ site.

hand, the Kondo effect is an important mechanism for controlling the impurity local moment. It is widely known that under Kondo temperature $T_K$ the impurity and conduction electrons form spin-singlet state, and in the meantime the local moment is totally screened. And the Kondo temperature is determined by the DOS on the Fermi surface, so with vanishing DOS on the Fermi surface near Dirac point the impurity behaves as free spin until temperature goes to zero. While in the case of Fermi surface far away from Dirac point the impurity local moment would be totally screened at finite temperature. However, the

recent experiment process does not allow us to change the Fermi energy of graphene arbitrarily and the tunable region is about [-1eV, 1eV], so we limit all of the calculation in this region.

## 5.3 Controlling the Impurity Moments by Tuning Fermi Energy of Graphene

We solve the problem using DQMC base on HF algorithm that allows us to deal with a nonconstant density of states for the host material and to avoid sign problem at low temperature [65]. To get primary insight, we examine the occupancy number $n_d = \langle d_\uparrow^\dagger d_\uparrow + d_\downarrow^\dagger d_\downarrow \rangle$ and impurity local moment $m_d^2 \equiv \langle (d_\uparrow^\dagger d_\uparrow - d_\downarrow^\dagger d_\downarrow)^2 \rangle$ as we tune the chemical potential $\mu$. In Fig. 5.2(a) and (b) we present the results of $n_d$ and $m_d^2$ versus $\mu$, respectively. They are obtained at low temperature $1/T = 128|t|^{-1}$. We apply the hole-particle symmetry $\varepsilon_d = -U/2$ and different values of hybridization. For small hybridization $V = 0.5|t|$ the occupancy and

local moment are almost independent of $\mu$, suggesting that the impurity decouples with graphene in the region $-3|t| \leq \mu \leq 0$. While for medium and large hybridization, we can tune occupancy and local moment through changing chemical potential in the region $[-0.3|t|, 0]$. It is interesting that for different values of hybridization the tunable regions for $n_d$ and $m_d^2$ are not fixed, which means that the renormalized energy $\tilde{\varepsilon}_d$ would shift as $V$ changes. Later we will see this point from spectral density of impurity. It is clear that when $-3|t| \leq \mu \leq 0$, the change of impurity local moment is very limited. So we examine the screening of conduction electrons for the local moment.

We calculate the spin susceptibility of impurity $\chi(T) = \int_0^\beta d\tau < m_d(\tau)m_d(0) >$, where $\beta = 1/T$ and $m_d(\tau) = e^{H\tau}m_d(0)e^{-H\tau}$. In Fig. 5.3(a) we show temperature timing spin susceptibility $T\chi(T)$ versus $\log T$ with hole-particle symmetry $\varepsilon_d = -U/2$. And in term of Clogston-Anderson *compensation theorem* [87] $T\chi(T)$ is screened moment which includes impurity local mo-

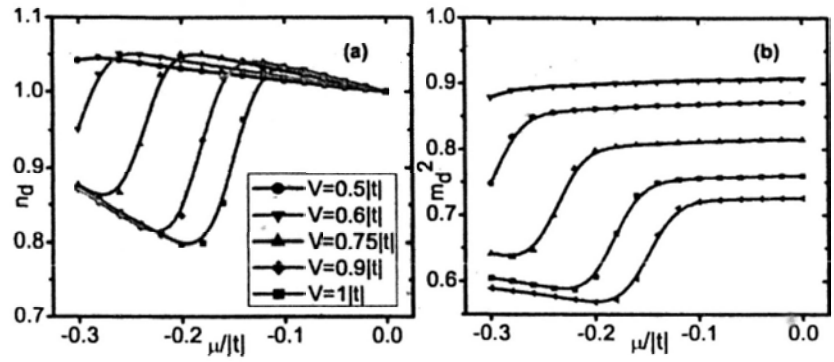


Figure 5.2: (Color online). (a) Occupancy $n_d$ versus chemical potential of graphene $\mu$, and (b) Local moment $m_d^2$ versus chemical potential of graphene $\mu$. In two figures, $U = 0.8|t|$, $\varepsilon_d = -U/2$ and the hybridizations are the same.

ment and spin correlation function between impurity and conduction electrons. In Fig. 5.3(a) at high temperature the $T\chi(T)$ approaches to a constant 0.5. As the temperature is lowered to $1/T = 64|t|^{-1}$, when chemical potential $\mu = 0, -0.1|t|$, $T\chi(T)$ does not seem to vanish and in the meantime the local moment of impurity is conserved well. While in the case of $\mu$ is far away from Dirac point $T\chi(T)$ decays rapidly as lowering the temperature suggesting that impurity goes to Kondo region and local moment become screened. In Fig. 5.3(b) we present the results

screened moment $T\chi(T)$ versus $\mu$ with hole-particle symmetry and at lower temperature $1/T = 128|t|^{-1}$. Here, we still limit the calculations in the region for chemical potential $[-0.3|t|, 0]$. For hybridization $V = 0.5|t|, 0.6|t|$, $T\chi(T)$ is independent of $\mu$ while hybridization $V = 0.75|t|, 0.9|t|, |t|$, $T\chi(T)$ becomes tunable. Furthermore the screened moment $T\chi(T)$ changes form a finite value to zero which means that we can switch on and off the impurity local moment though tuning the chemical potential $\mu$ by gate voltage applied to graphene.

In normal metal with constant density of states with hole-particle symmetry, the Kondo temperature can be calculated as $T_K \propto \Gamma\sqrt{u}\exp(-\pi^2 u/8)$, here $u = U/\pi\Gamma$ and $\Gamma = \pi V^2\rho(\varepsilon)$ [88]. When spin susceptibility $T\chi(T)$ shows universal behavior at low temperatures, we can extract Kondo temperature $T_K$ using Wilson's criterion

$$T_K\chi(T_K) = 0.025. \tag{5.4}$$

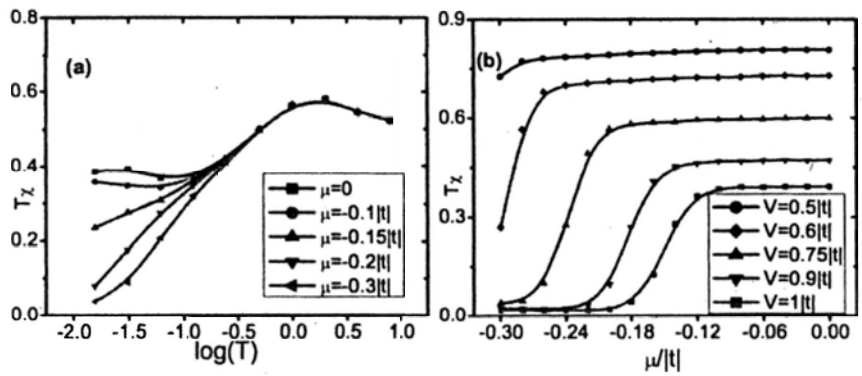


Figure 5.3: (Color online). (a) Temperature timing impurity spin susceptibility (screened moment) $T\chi$ versus $\log T$ for $\mu = 0$, $-0.1|t|$, $-0.15|t|$, $-0.2|t|$, $-0.3|t|$ and hybridization $V = 1.0|t|$. (b) $T\chi$ versus $\mu$ and the hybridizations for curves from top to bottom are $V = 0.5|t|$, $0.6|t|$, $0.75|t|$, $0.9|t|$ and $1.0|t|$. $U = 0.8|t|$ and $\varepsilon_d = -U/2$.

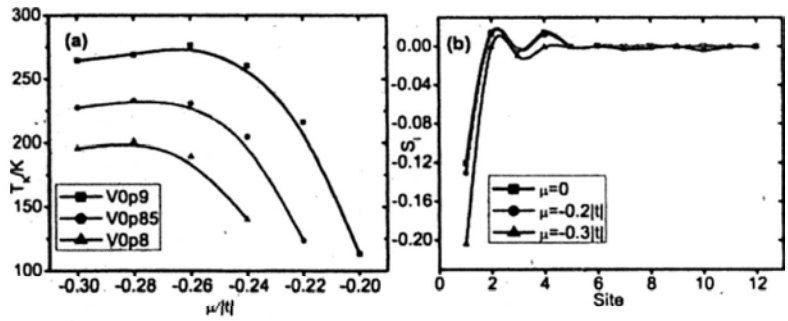


Figure 5.4: (Color online). In (a) Kondo temperature $T_K$ versus $\mu$ the hybridizations for curves from top to bottom are $V = 0.9|t|$, $0.85|t|$ and $0.8|t|$. (b) The spin correlation $S_i$ versus site $i$ for $\mu = 0$, $-0.2|t|$ and $-0.3|t|$ and hybridization $V = 0.75|t|$, and temperature $1/T = 64|t|^{-1}$. In (a)-(b), $U = 0.8|t|$ and $\varepsilon_d = -U/2$.

The results are shown in Fig. 5.4(a) where $T_K$ is a function of chemical potential $\mu$. When chemical potential is far away from Dirac point, Kondo temperatures become saturated and $T_K$ is higher as hybridization increases. We see that as $\mu$ shifts towards Dirac point the Kondo temperature decays rapidly. Kondo temperatures can be tuned in different regions of chemical potential $\mu$ with distinct values of hybridizations. To study the screening of impurity local moment, we calculate the spin correlation

function $S_i$ between impurity and electrons on the graphene lattices. Here, the correlation function is defined as $S_i \equiv \langle m_d m_i \rangle$, where $m_i$ is the, magnetic moment of the graphene atom. In Fig. 5.4(b), the first atom is the site which the impurity is located at. There is anti-ferromagnetic correlation between impurity and the on-site graphene atom, and as $\mu$ is farther from Dirac point the correlation increases. While when $\mu$ is near Dirac point the correlations of the nearest or next-nearest neighbors become larger, because in this case the graphene has strong anti-ferromagnetic correlation reduced by impurity. From the results of $n_d$, $m_d^2$, $T\chi(T)$ and $T_K$, we see that although the original parameters $\varepsilon_d$ and $U$ are the same, we can change these physical quantities in distinct regions of $\mu$ with different hybridizations. The possibility for us to control impurity is determined by the positions where renormalized energy levels of impurity are located, so it is necessary to study the spectral density of impurity.

## 5.4 Spectral Density of Impurity

From QMC based on HF algorithm, $A(\omega)$ is obtained by a maximum entropy analytic continuation of the imaginary-time Green's function[89, 90]. In Fig. 5.5, the temperature $1/T = 12|t|^{-1}$, for Trotter approximation $\Delta\tau = 0.25$, and for every subfigure $\varepsilon_d = -U/2$. In Fig. 5.5(a), we present results of $A(\omega)$ with different values of Coulomb interaction $U$. For transition metals in a metallic matrix, the Coulomb interaction is of the order of $\sim 5 - 10$ eV, here we do the calculations by $U \sim 3 - 5.5$ eV. Firstly, there is no Kondo peak at Fermi surface $\omega = 0$ because of vanishing DOS at Dirac point in graphene. And when Coulomb interaction $U$ increases the two peaks of $A(\omega)$ are separated further and broadened in the meantime the self-energy of impurity is enhanced due to the increase of DOS in graphene. Secondly, the maximums of $A(\omega)$, corresponding to levels for spin-up and spin-down electrons, are shifted from $\varepsilon_d$ and $\varepsilon_d + U$

and the energy difference $D$ between two peaks is much smaller than $U$, and the similar results have been obtained by numerical renormalization group method [55].

In Fig. 5.5(b), we present the results of $A(\omega)$ with different hybridizations $V$ and $\mu$ is located at the Dirac point. We see that when the hybridization increases, the two peaks of $A(\omega)$ shift towards the Dirac point and in the meantime the peaks become sharper suggesting the self-energy of impurity decreases. These behaviors are absolutely different from the case of impurity in normal metal. In normal metal, and above the Kondo temperature, the spectral density of impurity has two Lorentzian peaks centered at $\omega = \pm U/2$ with width $\Gamma = \pi V^2 \rho$. And when hybridization increases the centers of two peaks can not shift, at the same the peaks will collapse. In Fig. 5.5(c) we examine the case of impurity in doped graphene ($\mu = -0.15|t|$) the spectral density $A(\omega)$ is enhanced in the negative-$\omega$ zone and has the similar properties to those shown in Fig. 5.5(b). We propose

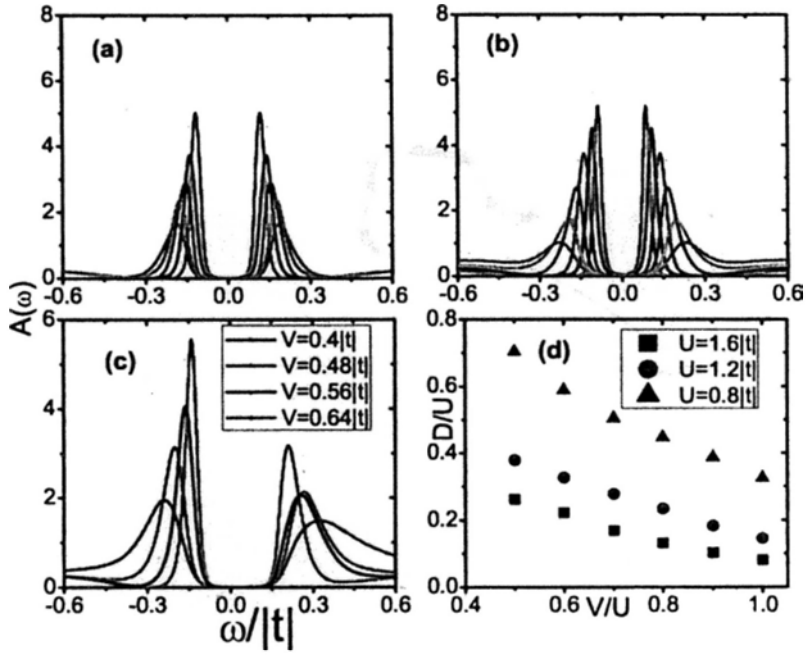


Figure 5.5: (Color online). (a) The spectral density of impurity $A(\omega)$ for $V = 0.96|t|$, $\mu = 0$ and from top to bottom, $U = |t|$, $1.2|t|$, $1.4|t|$, $1.6|t|$ and $1.8|t|$. (b)The spectral density of impurity $A(\omega)$ for $U = 1.2|t|$, $\mu = 0$ and the hybridizations, from top to bottom, are $V/U = 1$, 0.9, 0.8, 0.7, 0.6 and 0.5. (c) The spectral density of impurity $A(\omega)$ in the case of $\mu = -0.15|t|$ and $U = 0.8|t|$. (d) The energy difference between two peaks $D$ versus hybridization $V$ and here $D, V$ are unit of $U$. In (a)-(d) the orbital energy of impurity $\varepsilon_d = -U/2$.

a qualitative explanation of these unconventional behaviors of $A(\omega)$ as following. By Hartree-Fock theory spectral density of impurity with spin $\sigma$ is

$$A_\sigma(\omega) = \frac{1}{\pi} \frac{\Gamma(\omega)}{(\omega - \widetilde{E}_{\overline{\sigma}})^2 + \Gamma^2(\omega)} \tag{5.5}$$

here $\widetilde{E}_{\overline{\sigma}} = \varepsilon_d + U < n_{d,\overline{\sigma}} >$, $\Gamma(\omega) = \pi V^2 \rho(\omega)$ and the total density of states $A(\omega) = \frac{1}{2}\sum_\sigma A_\sigma(\omega)$. Firstly, we consider the parameters $\varepsilon_d$ and $\varepsilon_d + U$ are in the linear-DOS region, and then $\rho(\omega) = \alpha|\omega|$, and $\Gamma(\omega) = \alpha\pi V^2|\omega|$, here $\alpha = A_c/2\pi\hbar^2 v_F^2$, $A_c$ is the unit cell area and $v_F$ is Fermi velocity. It is easy to obtain that there are also two peaks for $A(\omega)$ at

$$\begin{aligned} \omega_1 &= \frac{\varepsilon_d}{\sqrt{1+\delta^2}}, \\ \omega_2 &= \frac{\varepsilon_d + U}{\sqrt{1+\delta^2}} \end{aligned} \tag{5.6}$$

here $\delta = \alpha\pi V^2$, and at the same time the values of the maximums for $A(\omega)$ are $1/\pi\Gamma(\omega_1)$ and $1/\pi\Gamma(\omega_2)$, so the two peaks of $A(\omega)$ have shifted from the bare parameters $\varepsilon_d$ and $\varepsilon_d + U$ and the distance between them is smaller than $U$. In graphene,

$A_c \sim 10^{-20}\mathrm{m}^2$, $v_F \sim 10^6\mathrm{ms}^{-1}$, and with $V \sim 1\mathrm{eV}$, we can estimate $\delta^2 \sim 10^{-4} \ll 1$. So in linear-DOS region, when the hybridization $V$ changes the shift of two peaks is not obvious. Secondly, beyond linear-DOS region and with medium or strong Coulomb interaction, we expand $\rho(\omega)$ around $\varepsilon_d$ to the first order $\rho(\omega) = \rho(\varepsilon_d) + \rho'(\varepsilon_d)(\omega - \varepsilon_d)$, then it is easy to extend the calculation through replacing $\alpha$ by $\rho'(\varepsilon_d)$. Using the analyze formula of $\rho(\omega)$ [51], in the region of $|\omega|$ from $0.5|t|$ to $0.8|t|$, $\rho'(\omega)$ has the order of $0.1 - 1\ \mathrm{eV}^{-2}$ so the term $\delta^2$ in Eq. (5.6) has the order of 1, and the shift of two peaks from $\varepsilon_d$ and $\varepsilon_d + U$ will become clear. So as hybridization increasing the renormalized energy level of impurity moves towards the Dirac point, and the self-energy of impurity decreases. In Fig. 5.5(d), we examine the energy difference $D$ in details. To compare with the case of impurity in normal metal $D = U$, we show the results of ratio $D/U$. We see that when the coulomb interaction $U$ is larger this kind of shift is more obvious: when $U = 0.8|t|$, $V = 0.4U$

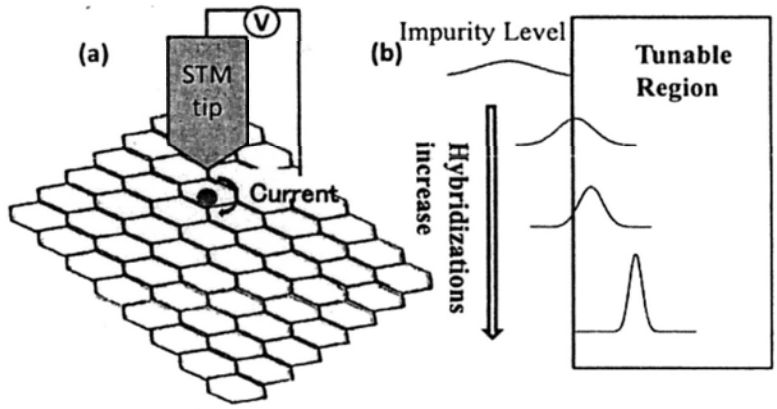


Figure 5.6: (Color online).(a) The schematic of STM tip is shown, and when a voltage is applied there is a current flowing from tip to impurity and graphene surface. In case of weak coupling for tip, the differential conductance is proportional to $A(\omega)$. (b) The recent experimentally tunable region of chemical potential $\mu$ is about [-1eV,1eV]. The possibility of controllability for impurity local moment is determined by the overlap between impurity levels and this tunable region. Large hybridization can push impurity levels into this region.

the difference $D$ is bout $70\%U$, while $U$ approaches to $1.6|t|$ the difference $D$ is only about $28\%U$.

The unconventional behaviors of spectral density are due to strong Coulomb interaction and large hybridization of impurity. These resonant levels can be directly measure by STM experi-

ments. In Fig. 5.6(a) it is shown the schematic of using STM tip to measure the spectral density of impurity and when a electric voltage is applied, there is a current flowing from the tip to the impurity and graphene. Considering the weak coupling between STM tip and graphene, the STM differential conductance at low temperature is given by [91, 92]

$$G(V_g) = \frac{4\pi e^2}{\hbar}\rho_t A(\mu + eV_g) \tag{5.7}$$

where $eV_g$ is the gate voltage drop from the tip to the sample, $\rho_t$ is the tip DOS at the Fermi energy which can be regarded as a constant and $A(\mu + eV_g)$ is the spectral density of impurity. So if the Fermi surface lying at the Dirac point the differential conductance is proportional to $A(eV_g)$. From the results of $A(\omega)$ in Fig. 5.5, we see that the Coulomb interaction is in the region $3 \sim 5.5$ eV and hybridization $1.1 \sim 5.5$ eV, and all the resonant levels are in the region $|\omega| < 1$ eV , which implies that the STM can measure these resonances. So firstly, the unconventional be-

haviors of spectral density let it easier to detect resonant levels of STM and it is not required that the bare parameters of impurity $\varepsilon_d$ and $\varepsilon_d + U$ are in the region $|\omega| \leq 1$ eV. Secondly, from the results of occupancy , local moment, screened moment and Kondo temperature versus chemical potential of graphene, we see that in the recent experimental process, and with small hybridization the physical properties of impurity are almost independent with $\mu$, while with medium and large hybridizations these physical quantities become tunable in different regions of $\mu$. The unconventional behaviors of $A(\omega)$ are good for us to control impurity local moment, especially, when the bare parameters of $\varepsilon_d$ and $\varepsilon_d + U$ are out of the tunable region which can be achieved by the recent experimental process.

---

□ **End of chapter.**

# Appendix A

# Tight-binding Spin Susceptibility

In this appendix, we provide detail derivation of the spin susceptibility of tight-binding model on the bilayer triangular lattice

$$\begin{aligned} & \left\langle c^{\dagger}_{\mathbf{k}_1 1\sigma}(\tau) c_{\mathbf{k}_2 1\sigma}(\tau) c^{\dagger}_{\mathbf{k}_3 1\sigma'} c_{\mathbf{k}_4 1\sigma'} \right\rangle \\ = & \frac{1}{4}\gamma_{\{\mathbf{k}\}} \left(A_1 + A_2 + A_3 + A_4 + A_5 + A_6\right) \end{aligned} \tag{A.1}$$

where

$$\gamma_{\{\mathbf{k}\}} = \frac{|\beta_{\mathbf{k}_1}||\beta_{\mathbf{k}_2}||\beta_{\mathbf{k}_3}||\beta_{\mathbf{k}4}|}{\beta_{\mathbf{k}_1}\beta^{*}_{\mathbf{k}_2}\beta_{\mathbf{k}_3}\beta^{*}_{\mathbf{k}4}}.$$

In the following we will calculate the six no-zero terms in

Eq.(A.1).

They are

$$\begin{aligned} A_1 &= \left\langle d^{\dagger}_{\mathbf{k}_1 1\sigma}(\tau) d_{\mathbf{k}_2 1\sigma}(\tau) d^{\dagger}_{\mathbf{k}_3 1\sigma'} d_{\mathbf{k}_4 1\sigma'} \right\rangle \\ &= e^{(E^{+}_{\mathbf{k}_1} - E^{+}_{\mathbf{k}_2})\tau} \big[ \langle n_{\mathbf{k}_1 1\sigma} \rangle \langle n_{\mathbf{k}_3 1\sigma'} \rangle \delta_{\mathbf{k}_1,\mathbf{k}_2} \delta_{\mathbf{k}_3,\mathbf{k}_4} \\ &\quad + \langle n_{\mathbf{k}_1 1\sigma} \rangle \langle 1 - n_{\mathbf{k}_2 1\sigma'} \rangle \delta_{\mathbf{k}_1,\mathbf{k}_4} \delta_{\mathbf{k}_2,\mathbf{k}_3} \delta_{\sigma,\sigma'} \big], \end{aligned} \tag{A.2a}$$

$$\begin{aligned} A_2 &= \left\langle d^{\dagger}_{\mathbf{k}_1 1\sigma}(\tau) d_{\mathbf{k}_2 1\sigma}(\tau) d^{\dagger}_{\mathbf{k}_3 2\sigma'} d_{\mathbf{k}_4 2\sigma'} \right\rangle \\ &= \langle n_{\mathbf{k}_1 1\sigma} \rangle \langle n_{\mathbf{k}_3 2\sigma'} \rangle \delta_{\mathbf{k}_1,\mathbf{k}_2} \delta_{\mathbf{k}_3,\mathbf{k}_4}, \end{aligned} \tag{A.2b}$$

$$\begin{aligned} A_3 &= \left\langle d^{\dagger}_{\mathbf{k}_1 1\sigma}(\tau) d_{\mathbf{k}_2 2\sigma}(\tau) d^{\dagger}_{\mathbf{k}_3 2\sigma'} d_{\mathbf{k}_4 1\sigma'} \right\rangle \\ &= e^{(E^{+}_{\mathbf{k}_1} - E^{-}_{\mathbf{k}_2})\tau} \langle n_{\mathbf{k}_1 1\sigma} \rangle \langle 1 - n_{\mathbf{k}_2 2\sigma} \rangle \\ &\quad \delta_{\mathbf{k}_1,\mathbf{k}_4} \delta_{\mathbf{k}_2,\mathbf{k}_3} \delta_{\sigma,\sigma'}, \end{aligned} \tag{A.2c}$$

$$\begin{aligned} A_4 &= \left\langle d^{\dagger}_{\mathbf{k}_1 2\sigma}(\tau) d_{\mathbf{k}_2 2\sigma}(\tau) d^{\dagger}_{\mathbf{k}_3 2\sigma'} d_{\mathbf{k}_4 2\sigma'} \right\rangle \\ &= e^{(E^{-}_{\mathbf{k}_1} - E^{-}_{\mathbf{k}_2})\tau} \big[ \langle n_{\mathbf{k}_1 2\sigma} \rangle \langle n_{\mathbf{k}_3 2\sigma'} \rangle \delta_{\mathbf{k}_1,\mathbf{k}_2} \delta_{\mathbf{k}_3,\mathbf{k}_4} \\ &\quad + \langle n_{\mathbf{k}_1 2\sigma} \rangle \langle 1 - n_{\mathbf{k}_2 2\sigma'} \rangle \delta_{\mathbf{k}_1,\mathbf{k}_4} \delta_{\mathbf{k}_2,\mathbf{k}_3} \delta_{\sigma,\sigma'} \big], \end{aligned} \tag{A.2d}$$

$$\begin{aligned} A_5 &= \left\langle d^{\dagger}_{\mathbf{k}_1 2\sigma}(\tau) d_{\mathbf{k}_2 2\sigma}(\tau) d^{\dagger}_{\mathbf{k}_3 1\sigma'} d_{\mathbf{k}_4 1\sigma'} \right\rangle \\ &= \langle n_{\mathbf{k}_1 2\sigma} \rangle \langle n_{\mathbf{k}_3 1\sigma'} \rangle \delta_{\mathbf{k}_1,\mathbf{k}_2} \delta_{\mathbf{k}_3,\mathbf{k}_4}, \end{aligned} \tag{A.2e}$$

$$
\begin{aligned}
A_6 &= \left\langle d^{\dagger}_{\mathbf{k}_1 2\sigma}(\tau) d_{\mathbf{k}_2 1\sigma}(\tau) d^{\dagger}_{\mathbf{k}_3 1\sigma'} d_{\mathbf{k}_4 2\sigma'} \right\rangle \\
&= e^{(E^{-}_{\mathbf{k}_1} - E^{+}_{\mathbf{k}_2})\tau} \left\langle n_{\mathbf{k}_1 2\sigma} \right\rangle \left\langle 1 - n_{\mathbf{k}_2 1\sigma} \right\rangle \\
&\quad \delta_{\mathbf{k}_1,\mathbf{k}_4} \delta_{\mathbf{k}_2,\mathbf{k}_3} \delta_{\sigma,\sigma'} . \qquad \text{(A.2f)}
\end{aligned}
$$

Because of $\delta$ function the factor $\gamma_{\{\mathbf{k}\}}$ equals to one.

After performing the integration over $\beta$ and sum over $R_{\mathrm{i}}$ and $R_{\mathrm{j}}$ the six terms become

$$
\begin{aligned}
&\frac{1}{N^3} \int_0^{\beta} d\tau \sum_{\mathbf{ij}} \sum_{\{\mathbf{k}\}} \frac{1}{4} \gamma_{\{\mathbf{k}\}} A_1 \\
&e^{i\mathbf{q}\cdot(R_{\mathrm{i}} - R_{\mathrm{j}}) + i(\mathbf{k}_1 - \mathbf{k}_2)\cdot R_{\mathrm{i}} + i(\mathbf{k}_3 - \mathbf{k}_4)\cdot R_{\mathrm{j}}} \\
&= \frac{\delta_{\sigma,\sigma'}}{4N} \sum_{\mathbf{k}_1} \frac{e^{\beta(E^{+}_{\mathbf{k}_1} - E^{+}_{\mathbf{k}_1+\mathbf{q}})} - 1}{E^{+}_{\mathbf{k}_1} - E^{+}_{\mathbf{k}_1+\mathbf{q}}} \left\langle n_{\mathbf{k}_1 1\sigma} \right\rangle \left(1 - \left\langle n_{\mathbf{k}_1+\mathbf{q} 1\sigma} \right\rangle\right) \\
&+ \frac{\delta_{\mathbf{q},\mathbf{0}}}{4N} \beta \sum_{\mathbf{k}_1,\mathbf{k}_3} \left\langle n_{\mathbf{k}_1 1\sigma} \right\rangle \left\langle n_{\mathbf{k}_3 1\sigma'} \right\rangle , \qquad \text{(A.3a)}
\end{aligned}
$$

we see that Eq. (A.3a) has two parts, the first part represents the correlation in band $E^{+}$, while the second part is only the

contribution of the point $\Gamma$ in band $E^+$.

$$\frac{1}{N^3}\int_0^\beta d\tau \sum_{\mathbf{ij}}\sum_{\{\mathbf{k}\}}\frac{1}{4}\gamma_{\{\mathbf{k}\}}A_2$$
$$e^{i\mathbf{q}\cdot(R_\mathbf{i}-R_\mathbf{j})+i(\mathbf{k}_1-\mathbf{k}_2)\cdot R_\mathbf{i}+i(\mathbf{k}_3-\mathbf{k}_4)\cdot R_\mathbf{j}}$$

$$= \frac{\delta_{\mathbf{q},\mathbf{0}}}{4N}\beta\sum_{\mathbf{k}_1,\mathbf{k}_3}\langle n_{\mathbf{k}_1 1\sigma}\rangle\langle n_{\mathbf{k}_3 2\sigma'}\rangle\,, \qquad \text{(A.3b)}$$

Eq. (A.3b) is only the correlation at point $\Gamma$ and describes the correlation between two bands. This term has no contributions to spin susceptibility.

$$\frac{1}{N^3}\int_0^\beta d\tau \sum_{\mathbf{ij}}\sum_{\{\mathbf{k}\}}\frac{1}{4}\gamma_{\{\mathbf{k}\}}A_3$$
$$e^{i\mathbf{q}\cdot(R_\mathbf{i}-R_\mathbf{j})+i(\mathbf{k}_1-\mathbf{k}_2)\cdot R_\mathbf{i}+i(\mathbf{k}_3-\mathbf{k}_4)\cdot R_\mathbf{j}}$$

$$= \frac{\delta_{\sigma,\sigma'}}{4N}\sum_{\mathbf{k}_1}\frac{e^{\beta(E^+_{\mathbf{k}_1}-E^-_{\mathbf{k}_1+\mathbf{q}})}-1}{E^+_{\mathbf{k}_1}-E^-_{\mathbf{k}_1+\mathbf{q}}}$$
$$\cdot\langle n_{\mathbf{k}_1 1\sigma}\rangle\left(1-\langle n_{\mathbf{k}_1+\mathbf{q}2\sigma}\rangle\right), \qquad \text{(A.3c)}$$

Eq. (A.3c) is the correlation of $E^+$ and $E^-$: the electrons not only occupy the lower band but also have possibility to occupy the upper band. The following three terms have the similar

forms:

$$\frac{1}{N^3}\int_0^\beta d\tau \sum_{\mathbf{ij}}\sum_{\{\mathbf{k}\}}\frac{1}{4}\gamma_{\{\mathbf{k}\}}A_4$$
$$e^{i\mathbf{q}\cdot(R_\mathbf{i}-R_\mathbf{j})+i(\mathbf{k}_1-\mathbf{k}_2)\cdot R_\mathbf{i}+i(\mathbf{k}_3-\mathbf{k}_4)\cdot R_\mathbf{j}}$$

$$= \frac{\delta_{\sigma,\sigma'}}{4N}\sum_{\mathbf{k}_1}\frac{e^{\beta(E^-_{\mathbf{k}_1}-E^-_{\mathbf{k}_1+\mathbf{q}})}-1}{E^-_{\mathbf{k}_1}-E^-_{\mathbf{k}_1+\mathbf{q}}}\left\langle n_{\mathbf{k}_1 2\sigma}\right\rangle\left(1-\left\langle n_{\mathbf{k}_1+\mathbf{q}2\sigma}\right\rangle\right)$$
$$+\frac{\delta_{\mathbf{q},0}}{4N}\beta\sum_{\mathbf{k}_1,\mathbf{k}_3}\left\langle n_{\mathbf{k}_1 2\sigma}\right\rangle\left\langle n_{\mathbf{k}_3 2\sigma'}\right\rangle, \tag{A.3d}$$

$$\frac{1}{N^3}\int_0^\beta d\tau \sum_{\mathbf{ij}}\sum_{\{\mathbf{k}\}}\frac{1}{4}\gamma_{\{\mathbf{k}\}}A_5$$
$$e^{i\mathbf{q}\cdot(R_\mathbf{i}-R_\mathbf{j})+i(\mathbf{k}_1-\mathbf{k}_2)\cdot R_\mathbf{i}+i(\mathbf{k}_3-\mathbf{k}_4)\cdot R_\mathbf{j}}$$

$$= \frac{\delta_{\mathbf{q},0}}{4N}\beta\sum_{\mathbf{k}_1,\mathbf{k}_3}\left\langle n_{\mathbf{k}_1 2\sigma}\right\rangle\left\langle n_{\mathbf{k}_3 1\sigma'}\right\rangle, \tag{A.3e}$$

$$\frac{1}{N^3}\int_0^\beta d\tau \sum_{\mathbf{ij}}\sum_{\{\mathbf{k}\}}\frac{1}{4}\gamma_{\{\mathbf{k}\}}A_6$$
$$e^{i\mathbf{q}\cdot(R_\mathbf{i}-R_\mathbf{j})+i(\mathbf{k}_1-\mathbf{k}_2)\cdot R_\mathbf{i}+i(\mathbf{k}_3-\mathbf{k}_4)\cdot R_\mathbf{j}}$$

$$= \frac{\delta_{\sigma,\sigma'}}{4N}\sum_{\mathbf{k}_1}\frac{e^{\beta(E^-_{\mathbf{k}_1}-E^+_{\mathbf{k}_1+\mathbf{q}})}-1}{E^-_{\mathbf{k}_1}-E^+_{\mathbf{k}_1+\mathbf{q}}}$$
$$\cdot\left\langle n_{\mathbf{k}_1 2\sigma}\right\rangle\left(1-\left\langle n_{\mathbf{k}_1+\mathbf{q}1\sigma}\right\rangle\right). \tag{A.3f}$$

We sum four terms of $\chi_{11}(\mathbf{q})$:

$$\langle n_{1\uparrow}(R_{\mathbf{i}},\tau)\, n_{1\uparrow}(R_{\mathbf{j}})\rangle - \langle n_{1\uparrow}(R_{\mathbf{i}},\tau)\, n_{1\downarrow}(R_{\mathbf{j}})\rangle$$

$$- \langle n_{1\downarrow}(R_{\mathbf{i}},\tau)\, n_{1\uparrow}(R_{\mathbf{j}})\rangle + \langle n_{1\downarrow}(R_{\mathbf{i}},\tau)\, n_{1\downarrow}(R_{\mathbf{j}})\rangle$$

and obtain Eq.(3.10).

For $\chi_{12}(\mathbf{q})$, the definition is similar to $\chi_{11}(\mathbf{q})$

$$\chi_{12}(\mathbf{q}) = \frac{1}{N}\int_0^\beta d\tau \sum_{\mathbf{ij}} e^{i\mathbf{q}\cdot(R_{\mathbf{i1}}-R_{\mathbf{j2}})} \langle m_1^z(R_{\mathbf{i1}},\tau) m_2^z(R_{\mathbf{j2}})\rangle\,, \quad \text{(A.4)}$$

where $R_{\mathbf{i1}}$ denotes the position of the atoms in the first layer and $R_{\mathbf{j2}}$ the second layer. We also note that $\chi_{12}(\mathbf{q})$ is independent of the related position of the two atoms in one unite cell. After derivations similar to $\chi_{11}(\mathbf{q})$, we obtain

$$\chi_{12}(\mathbf{q}) = C_1 + C_2 + C_3 + C_4, \quad \text{(A.5)}$$

which also has four terms, two came from intraband electrons and the other two came from interband electrons.

$$C_1 = \frac{-1}{4N}\sum_{\mathbf{k}\sigma} \frac{\langle n_{\mathbf{k+q}1\sigma}\rangle - \langle n_{\mathbf{k}1\sigma}\rangle}{E^+_{\mathbf{k+q}} - E^+_{\mathbf{k}}} e^{i(\varphi_{\mathbf{k+q}}-\varphi_{\mathbf{k}})} \quad \text{(A.6a)}$$

$$C_2 = \frac{1}{4N}\sum_{\mathbf{k}\sigma}\frac{\langle n_{\mathbf{k+q}1\sigma}\rangle - \langle n_{\mathbf{k}2\sigma}\rangle}{E^+_{\mathbf{k+q}} - E^-_{\mathbf{k}}}e^{i(\varphi_{\mathbf{k+q}}-\varphi_{\mathbf{k}})} \tag{A.6b}$$

$$C_3 = \frac{1}{4N}\sum_{\mathbf{k}\sigma}\frac{\langle n_{\mathbf{k+q}2\sigma}\rangle - \langle n_{\mathbf{k}1\sigma}\rangle}{E^-_{\mathbf{k+q}} - E^+_{\mathbf{k}}}e^{i(\varphi_{\mathbf{k+q}}-\varphi_{\mathbf{k}})} \tag{A.6c}$$

$$C_4 = \frac{-1}{4N}\sum_{\mathbf{k}\sigma}\frac{\langle n_{\mathbf{k+q}2\sigma}\rangle - \langle n_{\mathbf{k}2\sigma}\rangle}{E^-_{\mathbf{k+q}} - E^-_{\mathbf{k}}}e^{i(\varphi_{\mathbf{k+q}}-\varphi_{\mathbf{k}})} \tag{A.6d}$$

The phase factor came from the linear transformation of Eqs. (3.3a) and (3.3b), which was defined as

$$e^{i\varphi_{\mathbf{k}}} = \frac{\beta_{\mathbf{k}}}{|\beta_{\mathbf{k}}|}. \tag{A.7}$$

We have

$$e^{i(\varphi_{\mathbf{k+q}}-\varphi_{\mathbf{k}})} = \frac{1 + e^{i(\mathbf{k+q})\cdot(\vec{a_1}-\vec{a_2})} + e^{-i(\mathbf{k+q})\cdot\vec{a_2}}}{\left|1 + e^{i(\mathbf{k+q})\cdot(\vec{a_1}-\vec{a_2})} + e^{-i(\mathbf{k+q})\cdot\vec{a_2}}\right|} \cdot \frac{1 + e^{-i\mathbf{k}\cdot(\vec{a_1}-\vec{a_2})} + e^{i\mathbf{k}\cdot\vec{a_2}}}{\left|1 + e^{i\mathbf{k}\cdot(\vec{a_1}-\vec{a_2})} + e^{-i\mathbf{k}\cdot\vec{a_2}}\right|}.$$

---

□ **End of chapter.**

# Bibliography

[1] K. Takada, H. Sakurai, E. Takayama-Muromachi, F. Izumi, R. A. Dilanian, and T. Sasaki. Superconductivity in two-dimensional $CoO_2$ layers. *Nature*, 422(6927):53–55, 2003.

[2] D. J. Singh. Quantum critical behavior and possible triplet superconductivity in electron-doped $CoO_2$ sheets. *Phys. Rev. B*, 68(2):020503, Jul 2003.

[3] K.-W. Lee, J. Kuneš, and W. E. Pickett. Charge disproportionation and spin ordering tendencies in $Na_xCoO2$ . *Phys. Rev. B*, 70(4):045104, Jul 2004.

[4] Peihong Zhang, Weidong Luo, Marvin L. Cohen, and Steven G. Louie. Fermi surface of $Na_xCoO_2$. *Phys. Rev.*

*Lett.*, 93(23):236402, Nov 2004.

[5] Carsten Honerkamp. Instabilities of interacting electrons on the triangular lattice. *Phys. Rev. B*, 68(10):104510, Sep 2003.

[6] M. M. Korshunov, I. Eremin, A. Shorikov, V. I. Anisimov, M. Renner, and W. Brenig. Itinerant in-plane magnetic fluctuations and many-body correlations in $Na_xCoO_2$ . *Phys. Rev. B*, 75(9):094511, Mar 2007.

[7] N. Bulut, W. Koshibae, and S. Maekawa. Magnetic correlations in the hubbard model on triangular and kagomé lattices. *Phys. Rev. Lett.*, 95(3):037001, Jul 2005.

[8] Shi-Quan Su, Zhong-Bing Huang, Rui Fan, and Hai-Qing Lin. Numerical study of ferromagnetic fluctuations and pairing correlations in the single-band Hubbard model on the triangular lattice. *Phys. Rev. B*, 77(12):125114, Mar 2008.

[9] J. W. Lynn, Q. Huang, C. M. Brown, V. L. Miller, M. L. Foo, R. E. Schaak, C. Y. Jones, E. A. Mackey, and R. J. Cava. Structure and dynamics of superconducting $Na_xCoO_2$ hydrate and its unhydrated analog. *Phys. Rev. B*, 68(21):214516, Dec 2003.

[10] J. D. Jorgensen, M. Avdeev, D. G. Hinks, J. C. Burley, and S. Short. Crystal structure of the sodium cobaltate deuterate superconductor $Na_xCoO_2{\cdot}4xD_2O$ ($x \approx \frac{1}{3}$). *Phys. Rev. B*, 68(21):214517, Dec 2003.

[11] M. D. Johannes and D. J. Singh. Comparison of the electronic structures of hydrated and unhydrated $Na_x$ CoO2:The effect of $H_2O$ . *Phys. Rev. B*, 70(1):014507, Jul 2004.

[12] R. J. Xiao, H. X. Yang, and J. Q. Li. Influence of water concentration on the electronic band structure of the hydrated

$Na_{0.3}CoO_2{\cdot}yH_2O$ superconductor using a local spin density approximation. *Phys. Rev. B*, 73(9):092517, Mar 2006.

[13] Ryotaro Arita. Electronic structure of sodium cobalt oxide: Comparing mono- and bilayer hydrate. *Phys. Rev. B*, 71(13):132503, Apr 2005.

[14] Rajiv R. P. Singh and Norbert Elstner. Quantum phase transitions in the triangular-lattice bilayer Heisenberg model. *Phys. Rev. Lett.*, 81(21):4732–4735, Nov 1998.

[15] Richard T. Scalettar, Joel W. Cannon, Douglas J. Scalapino, and Robert L. Sugar. Magnetic and pairing correlations in coupled Hubbard planes. *Phys. Rev. B*, 50(18):13419–13427, Nov 1994.

[16] K. Bouadim, G. G. Batrouni, F. Hébert, and R. T. Scalettar. Magnetic and transport properties of a coupled Hubbard bilayer with electron and hole doping. *Phys. Rev. B*, 77(14):144527, Apr 2008.

[17] M. B. Stone, M. D. Lumsden, Y. Qiu, E. C. Samulon, C. D. Batista, and I. R. Fisher. Dispersive magnetic excitations in the $S = 1$ antiferromagnet $Ba_3Mn_2O_8$. *Phys. Rev. B*, 77(13):134406, Apr 2008.

[18] E. C. Samulon, Y.-J. Jo, P. Sengupta, C. D. Batista, M. Jaime, L. Balicas, and I. R. Fisher. Ordered magnetic phases of the frustrated spin-dimer compound $Ba_3Mn_2O_8$. *Phys. Rev. B*, 77(21):214441, Jun 2008.

[19] M. B. Stone, M. D. Lumsden, S. Chang, E. C. Samulon, C. D. Batista, and I. R. Fisher. Singlet-triplet dispersion reveals additional frustration in the triangular-lattice dimer compound $ba_3mn_{2O}8$. *Phys. Rev. Lett.*, 100(23):237201, Jun 2008.

[20] S. Bahr, C. J. Milios, L. F. Jones, E. K. Brechin, V. Mosser, and W. Wernsdorfer. Influence of antisymmetric exchange interaction on quantum tunneling of magnetiza-

tion in a dimeric molecular magnet $Mn_6$ . *Phys. Rev. B*, 78(13):132401, Oct 2008.

[21] K. S. Novoselov, A. K. Geim, S. V. Morozov, D. Jiang, M. I. Katsnelson, I. V. Grigorieva, S. V. Dubonos, and A. A. Firsov. Two-dimensional gas of massless Dirac fermions in graphene. *Nature*, 438(7065):197–200, 2005.

[22] Hal Tasaki. Stability of ferromagnetism in the Hubbard model. *Phys. Rev. Lett.*, 73(8):1158–1161, Aug 1994.

[23] R. Hlubina, S. Sorella, and F. Guinea. Ferromagnetism in the two dimensional $t - t'$ Hubbard model at the Van Hove density. *Phys. Rev. Lett.*, 78(7):1343–1346, Feb 1997.

[24] S. Daul and R. M. Noack. Ferromagnetic transition and phase diagram of the one-dimensional Hubbard model with next-nearest-neighbor hopping. *Phys. Rev. B*, 58(5):2635–2650, Aug 1998.

[25] T. Wegner, M. Potthoff, and W. Nolting. Temperature-dependent electronic structure and ferromagnetism in the $d = \infty$ Hubbard model studied by a modified perturbation theory. *Phys. Rev. B*, 57(11):6211–6214, Mar 1998.

[26] Liliana Arrachea. Itinerant ferromagnetism in the two-dimensional $t-t'$ Hubbard model. *Phys. Rev. B*, 62(15):10033–10037, Oct 2000.

[27] T. Koretsune and M. Ogata. Ferromagnetism on the frustrated lattices. *J. Phys. Soc. Jpn.*, 72(10):2437–2440, 2003.

[28] H. Q. Lin and J. E. Hirsch. Two-dimensional Hubbard model with nearest- and next-nearest-neighbor hopping. *Phys. Rev. B*, 35(7):3359–3368, Mar 1987.

[29] S. A. Wolf, D. D. Awschalom, R. A. Buhrman, J. M. Daughton, S. Von Molnar, M. L. Roukes, A. Y. Chtchelkanova, and D. M. Treger. Spintronics: A spin-based electronics vision for the future. *Science*, 294(5546):1488, 2001.

[30] K. Ando. Seeking room-temperature ferromagnetic semiconductors. *Science*, 312(5782):1883–1885, 2006.

[31] Igor Žutić, Jaroslav Fabian, and S. Das Sarma. Spintronics: Fundamentals and applications. *Rev. Mod. Phys.*, 76(2):323–410, Apr 2004.

[32] M. Dragoman and D. Dragoman. *Nanoelectronics: principles and devices.* Artech House Boston, 2006.

[33] Y. Zhang, Y. W. Tan, H. L. Stormer, and P. Kim. Experimental observation of the quantum Hall effect and Berry's phase in graphene. *Nature*, 438(7065):201–204, 2005.

[34] A. K. Geim and K. S. Novoselov. The rise of graphene. *Nature materials*, 6:183–191, 2007.

[35] T. Ohta, A. Bostwick, T. Seyller, K. Horn, and E. Rotenberg. Controlling the electronic structure of bilayer graphene. *Science*, 313(5789):951, 2006.

[36] C. L. Kane and E. J. Mele. Quantum spin hall effect in graphene. *Phys. Rev. Lett.*, 95(22):226801, Nov 2005.

[37] N. Tombros, C. Jozsa, M. Popinciuc, H.T. Jonkman, and B.J. Van Wees. Electronic spin transport and spin precession in single graphene layers at room temperature. *Nature*, 448(7153):571–574, 2007.

[38] K. S. Novoselov, A. K. Geim, S. V. Morozov, D. Jiang, Y. Zhang, S. V. Dubonos, I. V. Grigorieva, and A. A. Firsov. Electric field effect in atomically thin carbon films. *Science*, 306(5696):666, 2004.

[39] Yuanbo Zhang, Joshua P. Small, Michael E. S. Amori, and Philip Kim. Electric field modulation of galvanomagnetic properties of mesoscopic graphite. *Phys. Rev. Lett.*, 94(17):176803, May 2005.

[40] E. H. Hwang and S. Das Sarma. Quasiparticle spectral function in doped graphene: Electron-electron interaction

effects in arpes. *Phys. Rev. B*, 77(8):081412, Feb 2008.

[41] Annica M. Black-Schaffer and Sebastian Doniach. Resonating valence bonds and mean-field $d$ -wave superconductivity in graphite. *Phys. Rev. B*, 75(13):134512, Apr 2007.

[42] Carsten Honerkamp. Density waves and cooper pairing on the honeycomb lattice. *Phys. Rev. Lett.*, 100(14):146404, Apr 2008.

[43] Yongjin Jiang, Dao-Xin Yao, Erica W. Carlson, Han-Dong Chen, and JiangPing Hu. Andreev conductance in the $d+id'$ -wave superconducting states of graphene. *Phys. Rev. B*, 77(23):235420, Jun 2008.

[44] D. S. L. Abergel and Tapash Chakraborty. Long-range coulomb interaction in bilayer graphene. *Phys. Rev. Lett.*, 102(5):056807, Feb 2009.

[45] R. Hlubina, S. Sorella, and F. Guinea. Ferromagnetism in the two dimensional $t - t'$ Hubbard Model at the Van Hove

density. *Phys. Rev. Lett.*, 78(7):1343–1346, Feb 1997.

[46] S. Q. Su, Z. B. Huang, and H. Q. Lin. Monte Carlo studies of magnetism and superconductivity on the triangular lattice. *Journal of Applied Physics*, 103:07C717, 2008.

[47] N. M. R. Peres, M. A. N. Araújo, and Daniel Bozi. Phase diagram and magnetic collective excitations of the hubbard model for graphene sheets and layers. *Phys. Rev. B*, 70(19):195122, Nov 2004.

[48] N. M. R. Peres, F. Guinea, and A. H. Castro Neto. Coulomb interactions and ferromagnetism in pure and doped graphene. *Phys. Rev. B*, 72(17):174406, Nov 2005.

[49] Thereza Paiva, R. T. Scalettar, W. Zheng, R. R. P. Singh, and J. Oitmaa. Ground-state and finite-temperature signatures of quantum phase transitions in the half-filled hubbard model on a honeycomb lattice. *Phys. Rev. B*, 72(8):085123, Aug 2005.

[50] N. M. R. Peres, F. Guinea, and A. H. Castro Neto. Electronic properties of disordered two-dimensional carbon. *Phys. Rev. B*, 73(12):125411, Mar 2006.

[51] A. H. Castro Neto, F. Guinea, N. M. R. Peres, K. S. Novoselov, and A. K. Geim. The electronic properties of graphene. *Reviews of Modern Physics*, 81(1):109–162, 2009.

[52] R. Blankenbecler, D. J. Scalapino, and R. L. Sugar. Monte Carlo calculations of coupled boson-fermion systems. I. *Phys. Rev. D*, 24(8):2278–2286, Oct 1981.

[53] K. Sengupta and G. Baskaran. Tuning kondo physics in graphene with gate voltage. *Phys. Rev. B*, 77(4):045417, Jan 2008.

[54] Bruno Uchoa, Valeri N. Kotov, N. M. R. Peres, and A. H. Castro Neto. Localized magnetic states in graphene. *Phys. Rev. Lett.*, 101(2):026805, Jul 2008.

[55] P. S. Cornaglia, Gonzalo Usaj, and C. A. Balseiro. Localized spins on graphene. *Phys. Rev. Lett.*, 102(4):046801, Jan 2009.

[56] R. R. Santos. Introduction to quantum Monte Carlo simulations for fermionic systems. *Brazilian Journal of Physics*, 33:36–54, 2003.

[57] J. Hubbard. Electron correlations in narrow energy bands. *Proceedings of the Royal Society of London. Series A, Mathematical and Physical Sciences*, 276(1365):238–257, 1963.

[58] M. Suzuki. Quantum Monte Carlo Methods. *Solid State Sciences*, 74, 1986.

[59] J. E. Hirsch. Two-dimensional Hubbard model: Numerical simulation study. *Phys. Rev. B*, 31(7):4403–4419, Apr 1985.

[60] W. von der Linden. A quantum Monte Carlo approach to many-body physics. *Physics Reports*, 220(2-3):53–162, 1992.

[61] A. L. Fetter and J.D. Walecka. *Quantum theory of many-particle systems.* Dover Pubns, 2003.

[62] E. Y. Loh Jr, J. E. Gubernatis, W. Hanke, and Y. V. Kopaev. Electronic Phase Transitions. *by W. Hanke and Yu. V. Kopaev, Elsevier Science, New York*, 1992.

[63] K. Binder and D. W. Heermann. *Monte Carlo simulation in statistical physics: an introduction.* Springer Verlag, 2002.

[64] N. Metropolis, AW Rosenbluth, MN Rosenbluth, AH Teller, and E. Teller. Equations of state calculations by fast computing machines. *J. Chem. Phys*, 21:108, 1953.

[65] J. E. Hirsch and R. M. Fye. Monte carlo method for magnetic impurities in metals. *Phys. Rev. Lett.*, 56(23):2521–2524, Jun 1986.

[66] S. Doniach and E. H. Sondheimer. *Green's functions for solid state physicists.* Imperial College Pr, 1998.

[67] T. A. Gloor and F. Mila. Strain induced correlation gaps in carbon nanotubes. *The European Physical Journal B-Condensed Matter and Complex Systems*, 38(1):9–12, 2004.

[68] Igor F. Herbut. Interactions and phase transitions on graphene's honeycomb lattice. *Phys. Rev. Lett.*, 97(14):146401, Oct 2006.

[69] R. G. Parr, D. P. Craig, and I. G. Ross. Molecular orbital calculations of the lower excited electronic levels of benzene, configuration interaction included. *The Journal of Chemical Physics*, 18:1561, 1950.

[70] Dionys Baeriswyl, David K. Campbell, and Sumit Mazumdar. Correlations and defect energies. *Phys. Rev. Lett.*, 56(14):1509, Apr 1986.

[71] S. Reich, J. Maultzsch, C. Thomsen, and P. Ordejón. Tight-binding description of graphene. *Phys. Rev. B*, 66(3):035412, Jul 2002.

[72] Shi-Liang Zhu, Baigeng Wang, and L.-M. Duan. Simulation and detection of dirac fermions with cold atoms in an optical lattice. *Phys. Rev. Lett.*, 98(26):260402, Jun 2007.

[73] Chang-Yu Hou, Claudio Chamon, and Christopher Mudry. Electron fractionalization in two-dimensional graphenelike structures. *Phys. Rev. Lett.*, 98(18):186809, May 2007.

[74] Congjun Wu, Doron Bergman, Leon Balents, and S. Das Sarma. Flat bands and Wigner crystallization in the honeycomb optical lattice. *Phys. Rev. Lett.*, 99(7):070401, Aug 2007.

[75] A. Mielke. Ferromagnetism in the Hubbard model on line graphs and further considerations. *Journal of Physics A: Mathematical and General*, 24:3311–3321, 1991.

[76] Hal Tasaki. Ferromagnetism in the Hubbard models with degenerate single-electron ground states. *Phys. Rev. Lett.*, 69(10):1608–1611, Sep 1992.

[77] R. Arita, K. Kuroki, and H. Aoki. d-and p-wave superconductivity mediated by spin fluctuations in two- and three-dimensional single-band repulsive Hubbard model. *JOURNAL-PHYSICAL SOCIETY OF JAPAN*, 69(4):1181–1191, 2000.

[78] Sudhakar Pandey and Avinash Singh. Ferromagnetism in the $t - t'$ hubbard model: Interplay of lattice, band dispersion, and interaction effects studied within a goldstone-mode preserving scheme. *Phys. Rev. B*, 75(6):064412, Feb 2007.

[79] F. Schedin, A. K. Geim, S. V. Morozov, E. W. Hill, P. Blake, M. I. Katsnelson, and K. S. Novoselov. Detection of individual gas molecules adsorbed on graphene. *Nature materials*, 6(9):652–655, 2007.

[80] A. Das, S. Pisana, B. Chakraborty, S. Piscanec, SK Saha, UV Waghmare, KS Novoselov, HR Krishnamurthy,

AK Geim, AC Ferrari, et al. Monitoring dopants by Raman scattering in an electrochemically top-gated graphene transistor. *Nature Nanotechnology*, 3(4):210–215, 2008.

[81] Y. Zhang, T. T. Tang, C. Girit, Z. Hao, M. C. Martin, A. Zettl, M. F. Crommie, Y. R. Shen, and F. Wang. Direct observation of a widely tunable bandgap in bilayer graphene. *Nature*, 459(7248):820–823, 2009.

[82] G. H. Li, A. Luican, J. M. B. Lopes dos Santos, A. H. Castro Neto, A. Reina, J. Kong, and E. Y. Andrei. Observation of Van Hove singularities in twisted graphene layers. *Nature Physics*, 6(2):109–113, 2009.

[83] J. Zhou, Q. Wang, Q. Sun, XS Chen, Y. Kawazoe, and P. Jena. Ferromagnetism in Semihydrogenated Graphene Sheet. *Nano Lett*, 9(11):3867–3870, 2009.

[84] Håvard Haugen, Daniel Huertas-Hernando, and Arne Brataas. Spin transport in proximity-induced ferromagnetic

graphene. *Phys. Rev. B*, 77(11):115406, Mar 2008.

[85] Y. Wang, Y. Huang, Y. Song, X. Zhang, Y. Ma, J. Liang, and Y. Chen. Room-Temperature Ferromagnetism of Graphene. *Nano Lett*, 9(1):220–224, 2009.

[86] P. W. Anderson. Localized magnetic states in metals. *Phys. Rev.*, 124(1):41–53, Oct 1961.

[87] A. M. Clogston and P. W. Anderson. Compensation of ferromagnetic and antiferromagnetic contributions of covalant admixture in the polarization of free electrons by inner shell spins. *Bull. Am. Phys. Soc.*, 6:124, 1961.

[88] F. D. M. Haldane. Theory of the atomic limit of the Anderson model. I. Perturbation expansions re-examined. *Journal of Physics C: Solid State Physics*, 11:5015, 1978.

[89] R. N. Silver, J. E. Gubernatis, D. S. Sivia, and M. Jarrell. Spectral densities of the symmetric anderson model. *Phys. Rev. Lett.*, 65(4):496–499, Jul 1990.

[90] J. E. Gubernatis, Mark Jarrell, R. N. Silver, and D. S. Sivia. Quantum monte carlo simulations and maximum entropy: Dynamics from imaginary-time data. *Phys. Rev. B*, 44(12):6011–6029, Sep 1991.

[91] G. D. Mahan. *Many-particle physics.* Plenum Pub Corp, 2000.

[92] P. S. Cornaglia and C. A. Balseiro. Scanning tunneling microscopy conductance of kondo impurities on open and structured surfaces. *Phys. Rev. B*, 67(20):205420, May 2003.